Teresa Filipa Alexandre Baptista Duarte

Caracterização ótica de semicondutores de largo (WBS) e ultralargo (UWBS) hiato energético

Optical characterization of wide (WBS) and ultrawide (UWBS) bandgap semiconductors

Universidade de Aveiro
2022

Teresa Filipa Alexandre Baptista Duarte

Caracterização ótica de semicondutores de largo (WBS) e ultralargo (UWBS) hiato energético

Optical characterization of wide (WBS) and ultrawide (UWBS) bandgap semiconductors

"Rasgou-se a solidão e o
meu conforto:
nesta mesa, sou musa
de mim mesma"

— Ana Luísa Amaral

Teresa Filipa
Alexandre Baptista
Duarte

Caracterização ótica de semicondutores de largo (WBS) e ultralargo (UWBS) hiato energético

Optical characterization of wide (WBS) and ultrawide (UWBS) bandgap semiconductors

Dissertação apresentada à Universidade de Aveiro para cumprimento dos requisitos necessários à obtenção do grau de Mestre em Engenharia Física, realizada sob a orientação científica da Professora Doutora Teresa Maria Fernandes Rodrigues Cabral Monteiro, Professora Associada com Agregação do Departamento de Física da Universidade de Aveiro e da Doutora Joana Catarina Ferreira Rodrigues, Investigadora Doutorada (Nível 1) do Departamento de Física da Universidade de Aveiro.

Apoio financeiro do FEDER através do programa COMPETE 2020 e da FCT – Fundação portuguesa para a Ciência e Tecnologia através dos projetos PTDC/CTM-CTM/3553/2020, "DEOFET- Defect Engineered 2D Oxide Field Effect Transistors for efficient biosensing", i3N UIDB/50025/2020 & UIDP/50025/2020 & LA/P/0037/2020.

o júri / the jury

presidente / president	**Professor Doutor Leonel Marques Vitorino Joaquim** Professor Auxiliar do Departamento de Física da Universidade de Aveiro
arguente / examiner	**Professora Doutora Maria de Fátima Guimarães Cerqueira** Professora Auxiliar do Departamento de Física da Universidade do Minho
orientador / supervisor	**Professora Doutora Teresa Maria Fernandes Rodrigues Cabral Monteiro** Professora Associada com Agregação do Departamento de Física da Universidade de Aveiro

agradecimentos / acknowledgements

Tenho de começar por agradecer à minha incrível equipa de orientação, à Professora Teresa Monteiro e à Doutora Joana Rodrigues. Obrigado por toda a disponibilidade, paciência e simpatia ao longo deste trajeto. Obrigado por confiarem em mim e me darem vontade de ir mais além. Quero também agradecer à Doutora Joana Mendes pelas amostras que foram o que começou toda esta aventura.

Ao Professor Vitor Bonifácio por toda a ajuda ao longo dos meus anos universitários, desde o projeto ao clube do livro.

À minha fantástica equipa do dia-a-dia, à minha molécula, Pedro e Gusto. Obrigado por me aturarem, me apoiarem imensamente e serem os melhores amigos que Aveiro me poderia oferecer.

A todas as pessoas bonitas que tive a oportunidade de me cruzar graças a esta linda cidade, obrigado. Obrigado à Rita, ao Peixoto, aos Guis, ao Gabriel, ao Gonçalo, ao Rendeiro, ao Ricas, à Bárbara, à Maria, à Sofia, à Ema, à Eva, à Margarida e a tantos outros pela companhia, pelos risos e pelo apoio. Aos meus pedacinhos de terra por terem confiado em mim. Aos meus parceiros dos sonhos, Madalena, Marta, Carol, Luís e Fábio, uma gigantesco obrigado por me terem acompanhado nas experiências extra universidade.

Um enorme obrigado aos meus besties da terra mãe por toda a amizade estes anos apesar das minhas eventuais ausências. Aos de sempre, Inês, Rafael, Eloise, Carolina, Marta, João, Mafalda, Tisha, Teixeirinha.

Por fim, e o obrigado mais especial. Aos meus pais, avó e irmão. Obrigado por esta oportunidade tão maravilhosa, por acreditarem tanto em mim e por todo o amor. Obrigado por me deixarem sempre ser poema e o ocasional mau-feitio.

Palavras-chave β-Ga_2O_3, GaN, 4H-SiC, diamante, luminescência, defeitos, centros óticos

Resumo

Com as crescentes necessidades energéticas atuais surge a necessidade de obter dispositivos eletrónicos e optoelectrónicos mais eficientes. Os semicondutores de ultraelevado e elevado hiato energético (UWBS, WBS) são materiais promissores para cumprir com os requisitos destes dispositivos.
Nesta tese caracterizaram-se centros oticamente ativos em diferentes amostras de UWBS e WBS, que incluem camadas epitaxias crescidas por deposição química na fase de vapor (CVD) de β-Ga_2O_3, GaN e 4H-SiC, assim como diamante em volume. Para tal, utilizaram-se diferentes técnicas de espetroscopia ótica: Raman, transmitância, fotoluminescência (PL) e excitação da PL (PLE). As medidas de Raman permitiram determinar a fase cristalina dos semicondutores em análise e identificar estados de tensão nas epicamadas. A amostra de GaN (crescida em Al_2O_3) e a homoestrutura de 4H-SiC evidenciaram efeitos de tensão compressiva. Para a homoestrutura de β-Ga_2O_3 verificou-se não ser possível excluir efeitos de tensão, porém não foi possível identificar o tipo. A amostra de diamante em volume revelou ser de elevada qualidade cristalina. As energias de hiato das amostras crescidas por epitaxia foram determinadas por transmitância. Para a identificação dos defeitos luminescentes nas amostras e identificação do povoamento dos estados eletrónicos emissores, realizaram-se medidas de PL e PLE à temperatura ambiente. A análise da PL das amostras foi complementada com estudos a 14 K. No β-Ga_2O_3 observaram-se bandas de emissão no ultravioleta (UVL) e azul (BL). Paralelamente, detetou-se uma emissão vermelha devido à presença do contaminante de Cr^{3+} na estrutura. No GaN foi possível identificar, a presença da recombinação de excitões livres e ligados, e uma banda amarela (YL1). No 4H-SiC, à temperatura ambiente, identificaram-se duas bandas de recombinação no azul (BL) e verde (GL) de pares dador aceitador (DAP). A 14 K observaram-se excitões ligados ao N, o que permitiu pressupor que a BL observada possa ser uma sobreposição de diferentes recombinações DAP. Para além desta, foi observada uma banda de emissão no vermelho (RL) atribuída à sobreposição espectral de vários centros. Foram ainda estudados dois diamantes em volume (Bulk 1 e 2). Na amostra Bulk 1 identificou-se na região espectral do azul o centro N3. Na amostra Bulk 2 foi possível identificar na região espectral do verde o centro H3 e na vermelha o defeito NV^0.
Em suma, o trabalho realizado permitiu inferir quanto às propriedades estruturais e óticas das amostras de UWBS e WBS em análise, reconhecer os defeitos oticamente ativos nas amostras, alguns dos quais assumem um papel de relevo em termos da condutividade dos materiais e podem condicionar a resposta dos semicondutores em várias aplicações eletrónicas e optoelectrónicas.

Keywords β-Ga_2O_3, GaN, 4H-SiC, diamond, luminescence, defects, optical centres

Abstract

With the current growing energy needs arises the need to obtain more efficient electronic and optoelectronic devices. Ultrawide and wide bandgap semiconductors (UWBS, WBS) are promising materials to meet the requirements of these devices.

In this thesis we characterized optically active centres in different UWBS and WBS samples, which include epitaxial layers grown by chemical vapour phase deposition (CVD) of β-Ga_2O_3, GaN and 4H-SiC, as well as Bulk diamond. To this end, different optical spectroscopy techniques were used: Raman, transmittance, photoluminescence (PL) and PL excitation (PLE). Raman measurements allowed the determination of the crystalline phase of the semiconductors under analysis and the identification of stress states in the epilayers. The GaN (grown on Al_2O_3) and the 4H-SiC samples evidenced compressive stress effects. For the β-Ga_2O_3 it was not possible to exclude stress effects, but it was not possible to identify the type. The Bulk diamond sample was revealed to be of high crystalline quality. The bandgap energies of the epitaxially grown samples were determined by transmittance. For the identification of the luminescent defects in the samples and the identification of the emitting electronic states, PL and PLE measurements at room temperature were performed. The PL analysis of the samples was complemented with studies at 14 K. In the β-Ga_2O_3 emission bands were observed in the ultraviolet (UVL) and blue (BL) region. In parallel, a red emission was detected due to the presence of the Cr^{3+} contaminant in the structure. In the GaN sample, it was possible to identify the presence of recombination of free and bound excitons, and a yellow band (YL1). In 4H-SiC, at room temperature, two recombination bands were identified in the blue (BL) and green (GL) donor acceptor pair (DAP). At 14 K N-bounded excitons were observed, which allowed us to assume that the observed BL may be an overlap of different DAP recombinations. In addition to this, an emission band was observed in red (RL) attributed to the spectral overlap of several centres. Two Bulk diamonds (Bulk 1 and 2) were also studied. In the Bulk 1 sample the N3 centre was identified in the spectral region of blue. In Bulk 2 it was possible to identify in the green spectral region the H3 centre and in the red one the NV^0 defect.

In summary, the work carried out allowed us to infer about the structural and optical properties of the UWBS and WBS samples under analysis, to recognize the optically active defects in the samples, some of which assume a relevant role in terms of the conductivity of materials and can condition the response of semiconductors in various electronic and optoelectronic applications.

Contents

List of Figures

List of Tables

List of abbreviations

UWBS	ultrawide bandgap semiconductors
UV	ultra violet
IR	infrared
MSM	metal-semiconductor-metal
MLG	multilayer graphene
BV	breakdown voltage
MOSFET	metal-oxide-semiconductor field-effect transistor
SBD	Schottky barrier diode
JBSFET	junction barrier Schottky diode
SPND	Schottky *p*-*n* diodes
PND	*p*-*n* junction diodes
BZ	Brillouin zone
CB	conduction band
VB	valence band
DFT	density functional theory
WZ	wurtzite
HCP	hexagonal close packed
EPM	empirical pseudopotential method
LA	longitudinal acoustic
TA	transverse acoustic
LO	longitudinal optic
TO	transverse optic
β-Ga_2O_3	monoclinic gallium oxide
Ga_2O_3	gallium oxide
GaN	gallium nitride
SiC	silicon carbide
4H-SiC	4H-silicon carbide
LCAO	linear combination of atomic orbital
BZW	Bagayoko, Zhao and Williams
DFPT	density functional perturbation theory
DAP	donor-acceptor pair
e-A	electron-acceptor
PL	photoluminescence
PLE	photoluminescence excitation
RT	room temperature
CCD	charge coupled device
WBS	wide bandgap
PMT	photomultiplier tube
T_d	tetrahedral
O_h	octahedral
ZPL	zero phonon line
FCC	face centred cubic
UVL	UV luminescence
NBE	near-band-edge
GL	green luminescence
YL1	yellow luminescence
BL	blue luminesnce
RL	red luminescence
STH	self-trapped holes
STE	self-trapped excitons
V_O	O vacancies
V_{Ga}	Ga vacancy
G_i	interstitial Ga
C_N	carbon in a an nitrogen site
HSE	Heyd-Scuseria-Ernzerhof
FX	free excitons
O_N	O donor on the N site
Si_{Ga}	Si donor on the Ga site
B_{Si}	B impurity residing at the Si site
V_C	carbon vacancy
P	phosphorous
B	boron
N	nitrogen
DX	donor bound exciton
CVD	chemical vapour deposition
MOCVD	metal organic chemical vapour deposition
NIRL	near infrared luminescence
FWHM	full width at half maximum

Chapter 1

Introduction

1.1 Motivation

The innovation scale of semiconductors can be measured through its impact - it led to the emergence of new industries, professions, production methods, organizations, etc. Without solid-state electronics, one would not have such powerful computers, large-scale automation, satellite communications, the list is quite extensive. So it became clear that semiconductor science and technology have and continue to have a compelling impact on society [1].

Research in the field of semiconductors began in the mid-XIX century at a slow pace. The work initially carried out described the physical phenomena involving properties that would later be those considered of semiconductor materials. The first effect that can be linked to a semiconductor behaviour was an observation made by M. Faraday in 1833, measuring a negative temperature coefficient for silver sulphide (Ag_2S) [2]. Another crucial milestone was achieved in 1877 by Adams and Day [3], when they discovered the existence of the photovoltaic effect in a contact between a metal and selenium. That is the ability of a contact rectifier to generate an electromotive force when illuminated. Two years later, E. H. Hall described the Hall effect [4] - a voltage can be established between opposite faces of a crystal when it is placed in a magnetic field. This effect proved to be of great importance in ascertaining the mobility of charge carriers and determining which of these are the cause of conduction (electrons or holes), which essentially establishes if a semiconductor is type n or p. In 1930, B. Gudden recognized that semiconductor conductivity was mainly due to the impurities present (minority carriers) and not a property of the bulk material [5]. With the development of the first transistor, more than 70 years ago, semiconducting materials caused revolutionary alterations in the world. The gap width of these materials is a crucial factor in their evolution, being Si the first generation and gallium arsenide (GaAs) the second. Each generation shows unique physical characteristics and thus different applications that can vary from electronics to optoelectronics [6]. With high energy demands, there is also a growing interest in wide bandgap (WBS) and ultrawide bandgap semiconductors (UWBS) (semiconductors with bandgaps wider than 3.4 eV) since these are more efficient for some technological applications, such as radio-frequency electronics, deep ultra violet (UV) light-emitting diodes and detectors, ultrahigh-voltage power switches, and electronics for extreme environment applications [6–8]. Therefore, WBS and UWBS are considered emerging materials, despite displaying some research challenges, which leaves plenty of room for improvement in further research. Among the most interesting WBS and UWBS being researched nowadays, some have been highlighted as monoclinic gallium oxide (β-Ga_2O_3), gallium nitride (GaN), silicon carbide (SiC) (in particular 4H-silicon carbide (4H-SiC)), and diamond.

A promising application for β-Ga_2O_3 is deep UV solar blind detectors. These have a cut-off wavelength shorter than 280 nm and are insensitive to visible and infrared (IR) radiation. Since β-Ga_2O_3 has a cut-off wavelength in the 250-280 nm range, detection is possible over the full range of deep UV [9]. Another important factor is the possibility of producing

wafers at low costs. Photodetectors based on β-Ga_2O_3 can be categorized as photoconductors, metal-semiconductor-metal (MSM) photodetectors, Schottky photodiodes, and heterojunction photodetectors [10]. Kong *et al.* [11] reported a deep UV photodetector fabricated from the direct transfer of a layer of multilayer graphene (MLG) film on a *n*-type gallium oxide (Ga_2O_3) wafer. The electrical analysis performed revealed that the MLG-Ga_2O_3 heterojunction displayed rectifying characteristics under deep UV light illumination, being highly sensitive to wavelengths below 254 nm, with great stability and reproducibility. Nakagomi *et al.* [12] fabricated a deep UV photodiode based on heterojunction between β-Ga_2O_3 and *p*-GaN with good rectifying properties. The device's responsivity was very high for wavelengths below of 240 nm. Under reverse bias, the photocurrent increased linearly with the increase of the UV-light intensity. Another advantage is that these photodetectors allow multiband light detection, due to the use of two semiconductors with different bandgap energies. For example, Kalra *et al.* [13] fabricated a UV-A/UV-C detector based on a β-Ga_2O_3/GaN heterojunction that presented UV-A and UV-C multiband photodetection (with β-Ga_2O_3 biased positive). The Fermi levels of the *n*-type β-Ga_2O_3 and GaN layers were very close, thus the light detection occurred in both layers.

GaN is perhaps one of the most widely explored semiconductors - it has been epitaxially grown since the late 1960s [14] and in 2014 it was the focus of the Nobel prize in Physics [15]. GaN vertical devices have been attracting increased attention due to their high thermal performance, high breakdown voltage (BV) and high current density for a given chip size. However, the high cost and small diameter of GaN substrates hinders the development of these power devices. GaN-on-Si structure is an attractive option for this problem thanks to the low cost of Si substrates [16]. In 2014, Zhang *et al.* [17] demonstrated for the first time a GaN vertical Schottky and *p-n* diodes on Si substrates. This first result showed promising potential for low-cost high power vertical devices based on the GaN-on-Si structure. Since then, various approaches have been used to achieve cost-effective GaN-on-Si vertical devices. Zou *et al.* [18] reported a fully-vertical GaN *p-i-n* diodes using GaN-on-Si epilayers with a good Baliga's figure of merit (37.0 MW/cm^2) for this type of device grown on Si substrates. The *p-i-n* diode was obtained after wafer bonding, Si substrate removal, and *n*-electrode formation at the top of the device. After its passivation, the device presented low differential on-resistance (3.3 mΩ·cm^2 at 300 A/cm^2) and a BV of 350 V [18]. Liu *et al.* [19] reported a GaN-on-Si vertical transistor fabricated on a 6.7 μm-thick *n-p-n* heterostructure grown on silicon substrates. This device consists of trench-gate quasi-vertical metal-oxide-semiconductor field-effect transistor (MOSFET) with a GaN drift layer of 4 μm thickness and Si dopant concentration of 2×10^{16} cm^{-3}. It exhibited high electron mobility in the drift layer (720 cm^2/V·s), a high off-state BV (645 V with specific on-resistance of 6.8 mΩ·cm^2) and enhancement-mode operation with a threshold voltage of 6.3 V and an on/off ratio of over 10^8 [19].

The research into SiC power devices dates back to the 1980's [20] and in 2001 the first commercially available SiC Schottky diode was introduced by Infineon [21]. Since then, there has been quite a growth in SiC technology and it has been used in several applications (solar, railway traction, electric vehicles, etc.) [21]. The development of SiC MOSFETs is of high interest for power device applications - they have been commercially introduced and it is expected that devices up to 3.3 kV will soon make the market and even higher voltage devices are being investigated [22]. Kawahara *et al.* [23] reported a 6.5 kV Schottky barrier diode (SBD) embedded SiC MOSFET free from bipolar degradation. The embedding of an SBD into each unit cell of SiC MOSFET allows to create a more compact integrated chip while maintaining device reliability - no bipolar current flows in any phase of the inverter operation, so the device does not suffer a reliability problem of bipolar degradation. The

device presented a high SBD current ($\sim$ 120 A/cm^2) and a stable threshold voltage [23]. Sung *et al.* [24] reported a monolithic integration of a 1.2 kV SiC MOSFET and junction barrier Schottky diode (JBSFET) with a device design that reduces the SiC wafer area. Because of the integration of the diode into the MOSFET structure on a single chip, the MOSFET and diode share the forward conducting layer and the edge termination region, which permits a significant reduction in SiC wafer area. Furthermore, this will also increase switching frequency thanks to the elimination of the parasitic inductance between separately packaged devices. Approaches like these, may reduce the number of packages used and thus decrease the cost of implementing SiC technologies in power converters [24].

Diamond has a number of alluring features, such as having the widest bandgap and highest thermal conductivity amongst semiconductors, which offers a tremendous potential for electronic applications. Despite this, diamond has the same problem as GaN - its substrates are still quite limited, not only in terms of availability and cost, but also the lack of shallow dopant species, which is one of the primary causes of poor room temperature performance of bulk diamond devices [25]. One of the many reported types of devices is Schottky *p*-*n* diodes (SPND). SPND's emerged as a way to overcome some of the weak points presented in SBD and *p*-*n* junction diodes (PND). The SPN, as its name indicates, is the combination of SBD and PND: it is constituted by a lightly phosphorous (P)-doped *n*-type layer sandwiched between highly boron (B)-doped *p*-type diamond layer and a Schottky metal [26]. A key factor in the improvement of diamond SPND is understanding the transport mechanism in the forward bias region [27]. Ozawa *et al.* [27] fabricated a SPND to determine the temperature dependence of the current-voltage (I-V) characteristics and examined the carrier transport. Using Richardson plots, they experimentally estimated the effective potential barrier on the hole current and reported that the thermionic emission current in the voltage region below the flat-band voltage could explain the carrier conduction mechanism. Moreover, their SPNDs with low P concentration in the *n*-type layer and a high B concentration in the p^+-type layer achieved high current density and low flat-band voltage [27]. Matsumoto *et al.* [28] reported the fabrication of SPNDs using a lightly nitrogen (N)-doped layer. In their paper, they focused on the use of N as a dopant since it is a widely available impurity in diamond. Despite N having a higher activation energy (1.7 eV) than P (0.57 eV), N doping is easier and safer. The devices reported presented high forward current density, rectification ratio and breakdown electric field at room temperature (RT). All of which indicates that an N-doped *n*-type layer is effective in SPNDs [28].

Though much work still needs to be conducted to improve the quality of WBS and UWBS devices, they are indeed promising materials.

1.2 Objectives and thesis organization

The main goal of this thesis is the characterization of optically active defects in WBS and UWBS matrices (β-Ga_2O_3, GaN, 4H-SiC and diamond). As previously explored, these WBS and UWBS are of high technological interest, hence the need to characterize these defects, which among other experimental techniques, can be inferred through spectroscopic techniques.

This thesis is organized into five main chapters, with the first one being the introduction and motivation of this work. The second chapter presents the structural, electronic and vibrational properties of the materials that were studied, while chapter three is dedicated to the optical characterization techniques. Chapter four is focused on the obtained results and the corresponding analysis and discussion. Finally, chapter five presents the main conclusions and some future work possibilities.

Chapter 2

Structural, electronic and vibrational properties of WBS and UWBS

2.1 Gallium oxide, β-Ga_2O_3

Gallium oxide presents six different types of polymorphs with unique characteristics: α, β, γ, δ, ε, and κ. In this work, we will only focus on its monoclinic phase, β-Ga_2O_3. The monoclinic phase of gallium oxide is the most thermodynamically stable (Figure 2.1) and it belongs to the space group C_{2h}^3-C2/m with lattice constants $a = 12.2$ Å; $b = 3.0$ Å; $c = 5.8$ Å [10]. The angle between a and c is approximately 140° [10]. The unit cell contains two crystallographically different Ga cations and three anions sites. Half of the Ga cations are in distorted tetrahedral coordination, and the other in distorted octahedral coordination. The O anions are packed into a distorted cubic structure. Thus, it is possible to verify different binding environments: tetrahedral (T_d) and octahedral (O_h). The low crystallographic symmetry of the monoclinic phase leads to anisotropy of optical and electric properties. Usually, the planes (001) and ($\bar{2}$01) are the most used for crystal surfaces for device applications and thin film growth [29]. The melting temperature for this polymorph is 1725 °C [30].

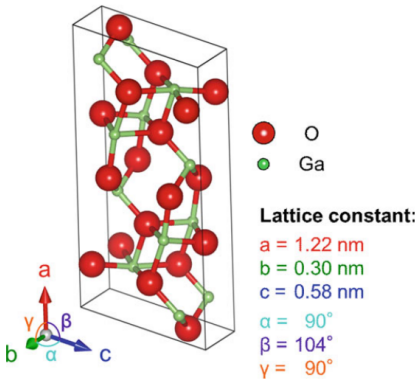

Figure 2.1: Schematic representation of the unit cell of β-Ga_2O_3 [10].

Utilizing the pseudopotential method and plane waves it is possible to obtain the β-Ga_2O_3 electronic band structure [31], as seen in Figure 2.2.
Monoclinic gallium oxide is considered as a direct bandgap semiconductor, with a bandgap of 4.87 eV at the Γ point, even though it exhibits also an indirect bandgap of 4.83 eV (M-Γ) [29]. The conduction band (CB) minimum is in the central zone of first Brillouin zone (BZ), at Γ point (**k**=**0**), being mainly composed of delocalized Ga 4s states. Therefore, the dispersive band has a low electron effective mass. The valence band (VB) is essentially formed by occupied O $2p^6$ derived states with minor hybridization with Ga 3d, 4p and 4s orbitals. It

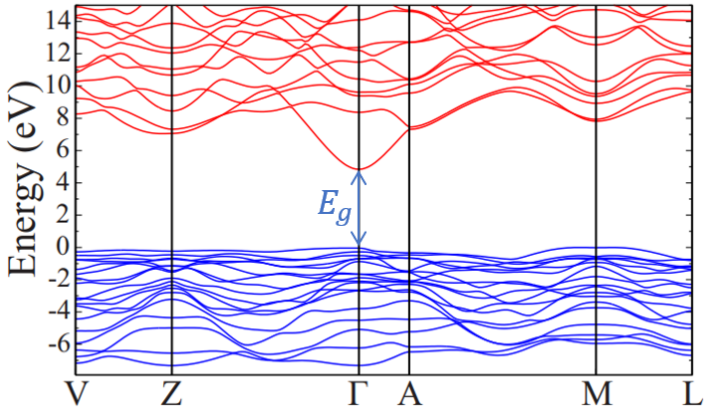

Figure 2.2: Electronic band structure for β-Ga_2O_3 along the high symmetry points and directions of the first BZ. Adapted from [31].

should be noticed that the top of the VB is predominantly composed of localized O 2p orbitals that exhibit quite low dispersion, resulting in a large hole effective mass [29].

Monoclinic gallium oxide has 10 atoms in its unit cell, which means that there are 30 phonon modes. Its point group is C_{2h} [32]. Figure 2.3 presents the phonon dispersion curves for β-Ga_2O_3 determined by density functional theory (DFT) calculation [10]. The irreducible representation of the acoustic modes in the centre of the first BZ is $\Gamma_{ac} = A_u + 2B_u$, while for the optical modes one has $\Gamma_{opt} = 10A_g + 4A_u + 5B_g + 8B_u$. A_g and B_g are active in Raman, while A_u and B_u are active in IR [33].

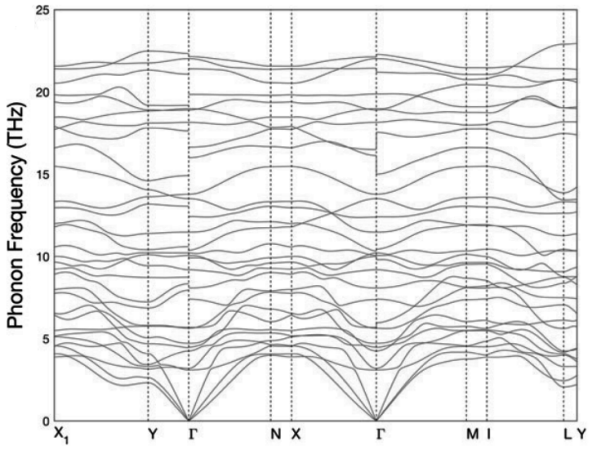

Figure 2.3: Phonon dispersion curves for β-Ga_2O_3 along some high symmetry points and directions of the first BZ. Adapted from [10].

2.2 Gallium nitride, GaN

Group-III nitrides, such as GaN, may present three types of crystalline structures: a) zincblende (spatial group $F\bar{4}3m$ (T_d^2)); b) wurtzite (WZ) (spatial group $P6_3mc$ (C_{6v}^4)); and c) rocksalt (spatial group $Fm3m$ (O_h^5)) [34]. Figure 2.4 presents a schematic representation

of the WZ structure, which will be the focus on this work since it is the most stable of the three.

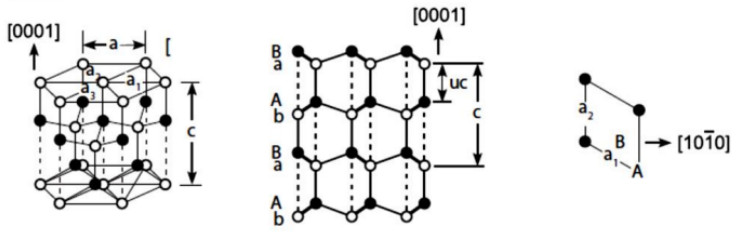

Figure 2.4: Crystalline structure of WZ GaN. In this figure, a closed circle represents a cation, an open circle an anion, a thick solid line denotes the projection of two bonds and the dash lines correspond to the connection of cations and anions pairs along the [0001] direction. Adapted from [35].

As mentioned above, GaN is typically found in the hexagonal modified WZ structure and the unit cell contains four atoms. This structure consists of two interpenetrating hexagonal close packed (HCP) sub-lattices, each of which has a type of atom, offset throughout the c axis of 3/8, where c is one of the lattice constants (height) [34]. In this case, the stacking sequence of {0001} planes is AaBbAaBbAa... along the [0001] axis. This structure contains two cation-anion pairs, where the cation atom is tetrahedrally surrounded by four anions atoms and vice-versa [36]. Since this structure has a hexagonal unit cell, it will have two lattices constants: a and c. The relationship between these two is as follows: $c/a = \sqrt{8/3} \approx 1.633$. The internal parameter, $u = 3/8 = 0.375$, corresponds to the length of the bonds parallel to [0001] in an ideal wurtzite cell. It is believed that the electrostatic interaction between the pairs of cation and anion atoms (connected by the dashed lines along the [0001] direction in Figure 2.4 (b)) is responsible for the higher stability of this structure over the other ones. Because of this effect, the ratio between c and a is actually lower than the ideal, while u is larger: $a = 3.189$ Å; $c = 5.185$ Å; $c/a = 1.626$; and $u = 0.376$ [35].

It is important to notice that none of the GaN structures has a centre of inversion, so describing an atom's position on a closed packed plane with coordinates (x, y, z) is different from describing it in the (-x, -y, -z) position. This absence of symmetry inversion causes the existence of crystallographic polarity. In general, the polar faces are the ones perpendicular to the c axis. For the WZ structure, the main polar planes are {0001} and {000$\bar{1}$} [36]. Furthermore, we can distinguish two orientations of GaN crystals - if the material is grown with Ga on top, then it is Ga-face (Figure 2.5a); but if it is grown with N on top, then it is N-face (Figure 2.5b). The Ga-face is considered to be inert whilst the N-face is chemically active. Since N has a higher electronegativity than Ga, the atoms in the crystal will present anionic and cationic characteristics, respectively, which results in a spontaneous polarization oriented along the c axis. This polarization depends on the asymmetry of the crystal - it increases with the decrease of the c/a ratio [37].

The empirical pseudopotential method (EPM) allows the determination of GaN electronic band structure. Although this method is not exact, EPM produces the complete band dispersion of the CB and VB and provides the necessary band structure parameters. Figure 2.6 presents the electronic band structure of WZ GaN obtained with EPM. The spin-orbit interaction was neglected [38]. The first Brillouin zone is a hexagonal prism with $2\pi/c$ height, where c is the lattice constant [35].

GaN is a direct bandgap semiconductor, with its band extremes located at the Γ point and a bandgap of 3.4 eV (at RT) [37]. The hexagonal symmetry induces a crystal field, in

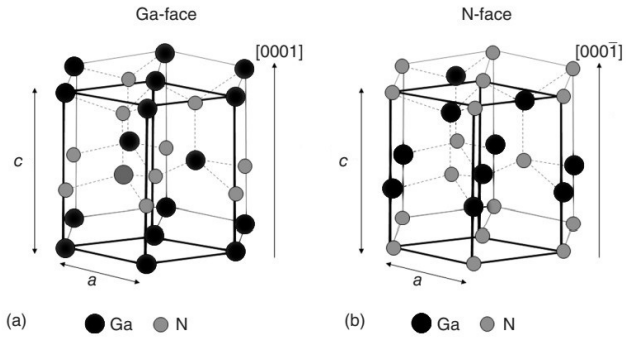

Figure 2.5: WZ structure for the Ga-face (a) and the N-face (b). In this figure, the bold lines are from the unit cell, while the dashed lines indicate the Ga-N bonds. Adapted from [37].

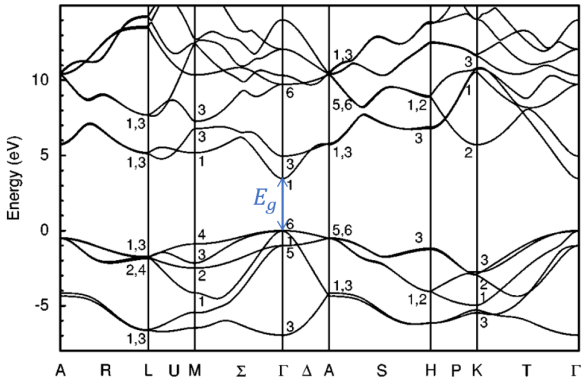

Figure 2.6: The electronic band structure of WZ GaN obtained with EPM, where spin-orbit interaction was neglected. The numbers present on the diagram correspond to the symmetry of the bands in the respective high-symmetry points and directions of the first BZ. The zero energy corresponds to the VB maximum. Adapted from [38].

which the splitting of the band states is due to the structural anisotropy between parallel to and normal to the c-axis [35]. The CB is nondegenerate and the lowest band consists mostly of s-like states. The VB, on the other hand, splits from the combination of spin-orbit interaction and the crystal field. It arises from N 2s, 2p and Ga 4s and 4p states. On the proximity of its maximum, it mainly comprises p-like states. Both the crystal field and the spin-orbit perturbations lead to degeneracy lifting. If one only considers the crystal field, the lowest energy band in CB is nondegenerated (Γ_1) and the upper band in VB is twofold-degenerated (Γ_6 symmetry). The hole effective mass in the upper three states of the VB is strongly dependent on the $\mathbf{k}$ wavevector [36].

The WZ structure has four atoms in its unit cell, leading to 12 phonon modes. Of these modes one is longitudinal acoustic (LA), two are transverse acoustic (TA), three are longitudinal optic (LO) and six are transverse optic (TO) [36]. Its spatial group is $C_{6\nu}^4$ and group theory predicts the following set of phonon modes (Γ point): $\Gamma = 2A_1+2E_1+2B_1+2E_2$, with $\Gamma_{opt} = A_1 + 2B_1 + E_1 + 2E_2$ and $\Gamma_{ac} = A_1 + E_1$. A_1, E_1 and E_2 are Raman active with A_1 and E_1 also IR active. Because the B_1 mode is not active neither in Raman nor IR, it is called silent mode [39]. While modes A and B are non degenerate, the E mode is doubly degenerate. Additionally, the A_1 and E_1 modes are polar, meaning that their vibrations polarize the unit cell, creating a long-range electrostatic field. The splitting of the A_1 and

E_1 modes in LO and TO is a consequence of this field [40]. Figure 2.7 presents the phonon dispersion curves determined by inelastic X-ray scattering and *ab initio* lattice-dynamical calculations [41].

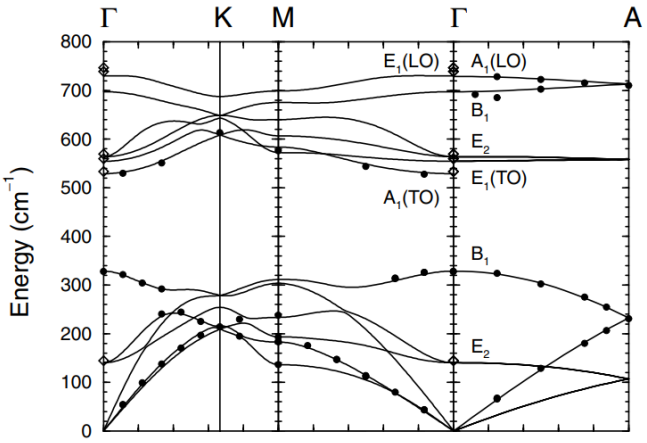

Figure 2.7: Phonon dispersion curves for WZ GaN along high-symmetry points and directions in the first BZ. The filled circles represent the phonon energies from inelastic X-ray scattering. Adapted from [41].

2.3 Silicon carbide, 4H-SiC

Silicon carbide (SiC) is a semiconductor that exists in over 200 different crystal forms [42], since any variation of the occupation sites along the c axis gives rise to a particular crystal structure - the polytypes. Depending on the number of stacked Si-C layers in the unit cell and the crystal system present, a specific designation is given to each polytype [42]. For example, in 4H-SiC there are four layers and the system is hexagonal, which is the polytype of focus in this work. It belongs to the point group $C_{6v}^4 - P6_3mc$ and has two lattice constants: $a = 3.076$ Å and $c = 10.05$ Å at 300 K [43]. The stacking sequence is ABAC (Figure 2.8). Since hexagonal polytypes are composed of stacked double layers, they present anisotropy [44].

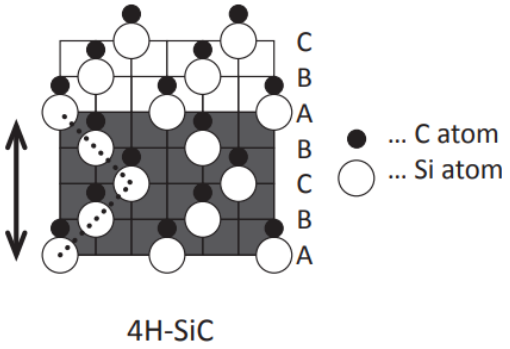

Figure 2.8: Arrangement of Si and C atoms for 4H-SiC, where A, B and C are the occupation sites of the hexagonal close-packed structure. Adapted from [42].

All SiC polytypes are indirect bandgap semiconductors with the maximum of the upper VB at the Γ point [43]. The band structure of these semiconductors can be studied using

different computational methods. For 4H-SiC, they usually involve DFT. The band diagram depicted in Figure 2.9, was obtained by Zhao *et al.* [45] using DFT, the linear combination of atomic orbital (LCAO) method and the Bagayoko, Zhao and Williams (BZW) procedure. The indirect bandgap energy estimated was 3.11 eV, which is close to the experimental data reported of 3.3 eV (at RT) obtained by soft X-ray spectroscopy [46]. In this case, the CB minimum is at the M-point [45]. There is also a direct bandgap of 4.80 eV at the M point [47].

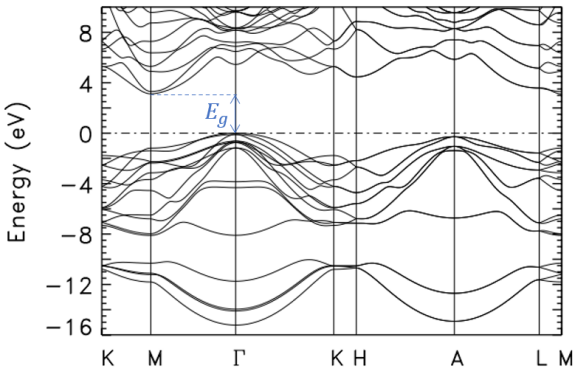

Figure 2.9: Electronic band structure of 4H-SiC along the high symmetry points and directions of the first BZ, obtained with the BZW procedure. Adapted from [45].

4H-SiC belongs to the $C_{6\nu}^4$ space group and has 8 atoms per unit cell, leading to a total of 24 phonon modes [48]. Figure 2.10 presents the phonon dispersion curves for 4H-SiC obtained by *ab initio*, DFT and density functional perturbation theory (DFPT) calculations [49]. The optical modes (at the Γ point) are given by $\Gamma_{opt} = 3A_1 + 4B_1 + 3E_1 + 2E_2$, where A_1, E_1 and E_2 are Raman active, A_1 and E_1 are also IR active and B_1 is a silent mode [50].

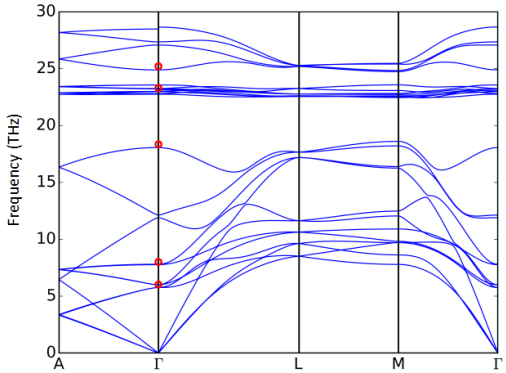

Figure 2.10: Phonon dispersion curves for 4H-SiC in the principal symmetry points and directions of the first BZ. Adapted from [49].

2.4 Diamond, C

Diamond is a tridimensional structure composed of carbon atoms - that results from an infinite repetition of C-C sp^3 bonds [51]. It has a face centred cubic (FCC) structure with a two atoms base (or two FCC lattices offset by 1/4 of the central body diagonal of the

cube), with a lattice constant of $a = 3.567$ Å (at RT), and coordination number 4 (Figure 2.11a) [52]. The stacking sequence of the {111} planes is ABCABC... (Figure 2.11b) [53]. Its spacial point group is $O_h^7 - Fd\bar{3}m$.

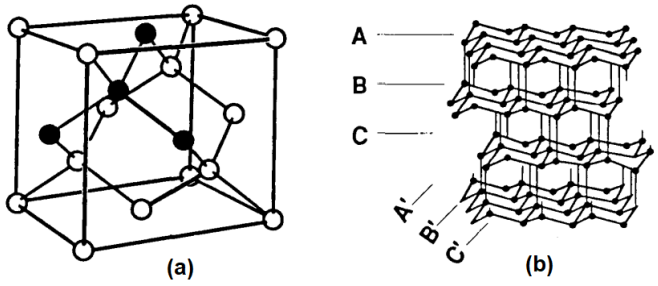

Figure 2.11: Schematics of (a) the diamond unit cell and (b) the stacking sequence of the {111} family of planes. Adapted from [53].

Pure diamond is constituted only by carbon atoms. However, it often presents substitutional and interstitial impurities in its lattice. Depending on the impurities present, diamond will have distinct properties from the pure form. Nitrogen is by far the most common impurity, so the basis of the classification for diamond is its presence or absence. Type I diamonds present sufficient N to be measurable while type II are practically free from impurities. Both of these classifications may be further divided into: a) Ia, contains N atoms in close proximity to one another; b) Ib, contains N atoms isolated from one another in the lattice (the N atoms replace C atoms in the lattice); c) IIa, the purest type; and d) IIb, contains B atoms (thought to be in a substitutional position) [54].

Figure 2.12 presents the electronic band structure for diamond obtained using LCAO method [55]. Diamond is an indirect bandgap semiconductor with a bandgap of 5.47 eV (at RT) [56], with the VB maximum at the Γ point and the CB minimum located along the [100] direction [57].

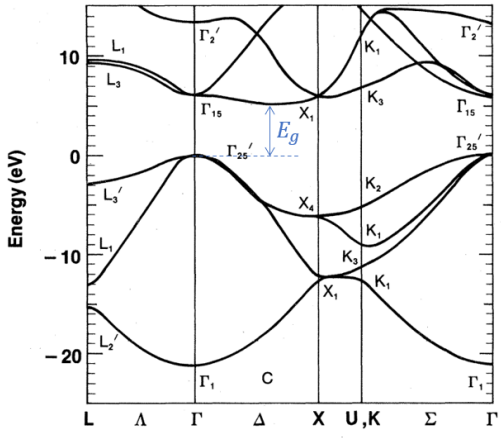

Figure 2.12: Electronic band structure for the diamond structure, where the top of the VB is taken as the zero of energy. High symmetry points and directions in the first BZ are indicated in the figure. Adapted from [55].

The set of VBs is composed of carbon 2s, 2p orbitals while the set of CBs is mostly composed of antibonding combinations of carbon 2s, 2p states and a minor combination of carbon 3s, 3p orbitals [58]. The VB maximum presents a set of three degenerate bands at the

Γ point. However, since the atomic number is small, the spin-orbit splitting of these bands at the Γ point is also small [57].

Diamond has a base with two atoms per primitive cell, which means that there will be 6 phonon modes [59]. From the selection rules of its factor group, O_h, T_{2g} is the only mode active in Raman and T_{1u} the only mode active in IR. Both of these modes are triply degenerate. Figure 2.13 presents the phonon dispersion curves for diamond obtained by inelastic neutron scattering [60].

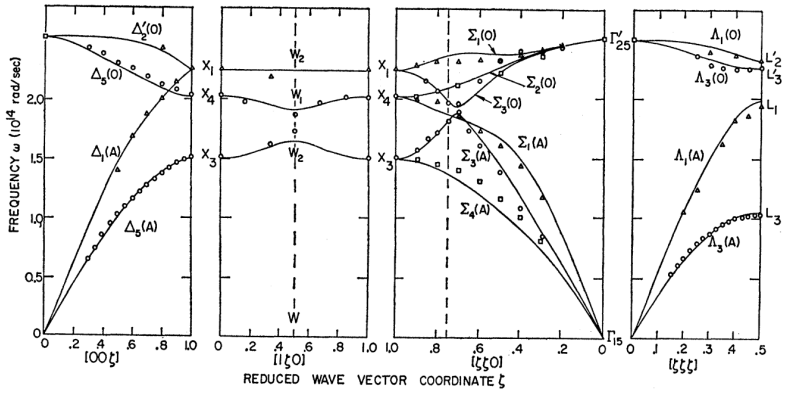

Figure 2.13: Phonon dispersion curves for diamond along the principal symmetry points and directions of the first BZ [60].

2.5 Important physical properties

Table 2.1 summarizes various relevant properties for these WBS and UWBS, in line with the discussion of the previous sections.

Table 2.1: Relevant physical properties of β-Ga_2O_3 [10, 29, 30, 61, 62], WZ GaN [36, 63], 4H-SiC [10, 25, 64, 65] and diamond [25, 66, 67] (at RT). D refers to direct, I to indirect, L to longitudinal and T to transverse.

Semiconductor		$\boldsymbol{\beta - Ga_2O_3}$	**GaN (WZ)**	**4H-SiC**	**Diamond**
E_g (eV)		4.87 (D)	3.4 (D)	3.3 (I)	5.47 (I)
Lattice constant (Å)	a	12.2	3.189	3.076	3.567
	b	3.0	-	-	-
	c	5.8	5.185	10.05	-
Melting temperature (^oC)		1725	2500	2740	3773
Thermal conductivity (W/cmK)		0.27	>2.1	3.7	22-24
Dielectric constant		10-12	8.9-9.5	9.7	5.7
Breakdown field (MV/cm)		>6	5	2.83	7.7-20
Effective mass (m_0)	e	0.28	0.20	0.29 (L) 0.42 (T)	1.4 (L) 0.36 (T)
	h	-	0.59	1.75 (L) 0.66 (T)	1.1
Mobility (cm^2/Vs)	e	153	∼1000	1000	1060
	h	-	≤ 200	120	2100

Chapter 3

Optical characterization: experimental techniques and theoretical concepts

3.1 Raman spectroscopy

When one illuminates a sample, photons may be transmitted, absorbed or scattered. In a pure semiconductor, for the light to be absorbed, it requires that the energy of the incident photons is equal or higher to the gap energy of the material. However, in the presence of defects, semiconductor samples may absorb smaller energies. On the other hand, scattering does not require a suitable pair of energy levels and it can be divided into three categories: Rayleigh, Brillouin and Raman scattering [68]. Rayleigh scattering is an elastic process, which means the scattered light has the same frequency as the incident beam (ω_0), as represented in Figure 3.1 (a) and (b). The other two processes are inelastic - Brillouin results from the interaction of the incident radiation with acoustic phonons while Raman is the result of the interaction with optical phonons [69]. The Raman scattering has frequencies $\omega_0 \pm \omega_m$, where ω_m is a vibrational frequency of the material. The line corresponding to $\omega_0 - \omega_m$ is called the Stokes line, while the one that appears at $\omega_0 + \omega_m$ is the anti-Stokes line [70]. Both scattering processes can be seen in Figure 3.1 (c). Figure 3.1 (d) shows the scattering phenomena (Rayleigh and Raman) in a schematic two energy level diagram, with the fundamental and first excited electronic levels represented by E_0 and E_1, respectively. The figure also depicts the vibrational levels n and m, where 0 is the ground and 1, 2, 3 are excited vibrational states. As we can see by this diagram, when the incident photon interacts with the lattice, it excites an electron from the lower vibrational state of the ground electronic level to a virtual electronic state (represented in the figure by the dashed lines). In most cases, the incident photon gives part of its energy to the lattice, resulting in the emission of a lower energy photon, and this is the Stokes case. However, if the lattice is in an excited vibrational state ($n > 0$), the scattering process can result in the emission of a photon with higher energy than the incident one [69]. This is the anti-Stokes case, and it occurs when the crystal already has a considerable density of phonons, which contributes to the occupation of vibrational levels with higher energy than the fundamental one, such as at high temperatures [36]. Since the anti-Stokes modes are much weaker than the Stokes ones, it is usually the Stokes modes that are monitored [69].

In Raman spectroscopy measurements, when the photon energy is equal to the difference between two real electronic levels, we have the resonant Raman [71]. When the excitation energy is lower than the bandgap, two things may happen: if the sample is a pure semiconductor, light is not absorbed between two real electronic states; however, if there are defects present, the semiconductor may absorb this smaller energy, as defects introduce levels in the bandgap (which is also a resonant Raman process).

This technique is highly useful as it allows the identification of vibrational modes. Because each material has specific lattice vibrational modes and energy positions for these, the Raman spectra can be used as a sort of fingerprint of a material. Furthermore, Raman spectroscopy also allows identifying strain effects, density of defects, alloy composition and crystallographic orientation, among other characteristics [36]. Raman spectroscopy is a non-destructive technique and, in most circumstances, the material can be analysed immediately in a microscope lamella. Its significant drawback is the interference induced by other signals like luminescence. Nonetheless, this can be reduced by utilizing nonresonant illumination, which allows the Raman spectrum to be measured without being obscured by the luminescence signal [36].

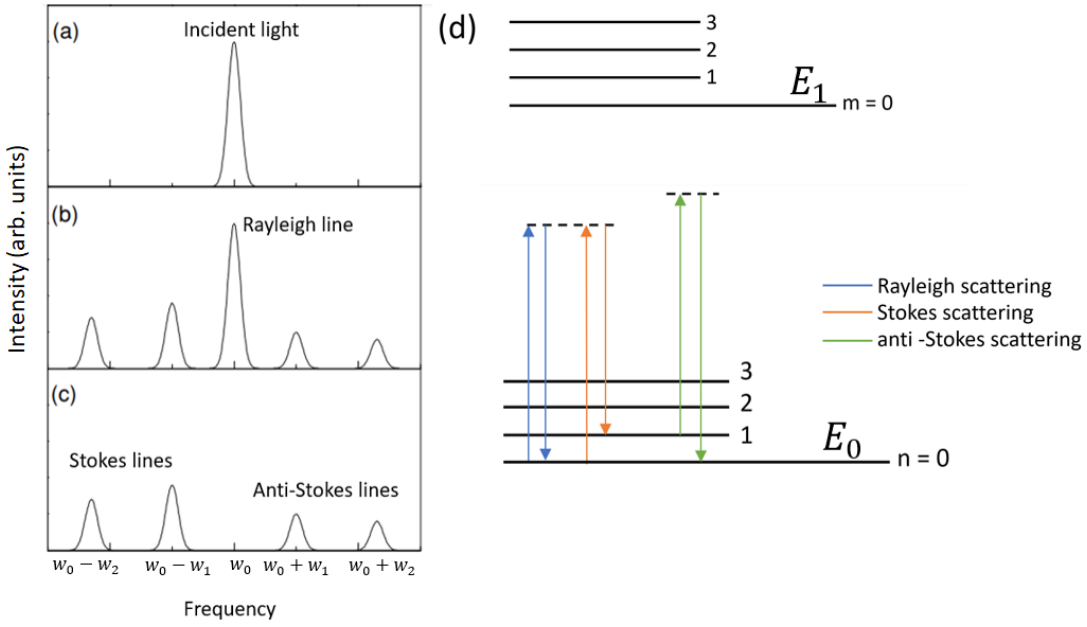

Figure 3.1: Representation of the spectra originated from (a) the incident light, (b) the scattered light (both Raman and Rayleigh), and (c) the contribution of the Raman spectrum. Adapted from [71]. (d) Two level energy diagram of the Rayleigh and Raman scattering processes, where the lines indicated with E represent the real electronic levels and the ones indicated with n, $m = 0, 1, 2, 3$ the vibrational states. The dashed lines represent the virtual electronic states.

To further understand the Raman effect, a classical theory approximation will be followed [70] and for additional simplification, vectorial notation will not be used. The electric field strength (E) of the electromagnetic radiation (laser beam) is given by the following equation:

$$E = E_0 cos(2\pi\omega_0 t) \tag{3.1}$$

where E_0 is the electric field amplitude, ω_0 the frequency of the laser and t the time. Assuming a diatomic molecule as an example, upon irradiation with this laser beam, an electrical dipole moment (P) is induced:

$$P = \alpha E = \alpha E_0 cos(2\pi\omega_0 t) \tag{3.2}$$

where α is the polarizability. If the molecule is vibrating with a given frequency ω_m, the nuclear displacement (Q) is given by:

$$Q = Q_0 cos(2\pi\omega_m t) \tag{3.3}$$

where Q_0 is the vibrational amplitude. If the vibration is of small amplitude, α is a linear function of Q, and thus:

$$\alpha = \alpha_0 + \left(\frac{\partial \alpha}{\partial Q}\right)_0 Q_0 + ... \tag{3.4}$$

where α_0 is the polarizability at the equilibrium position and $(\partial\alpha/\partial Q)_0$ is the rate of change of α when Q is in the equilibrium position. Combining equations 3.1, 3.2 and 3.3 one can write

$$P = \alpha_0 E_0 cos(2\pi\omega_0 t) + \frac{1}{2}\left(\frac{\partial \alpha}{\partial Q}\right)_0 Q_0 E_0 [cos\{2\pi(\omega_0 + \omega_m)t\} + cos\{2\pi(\omega_0 - \omega_m)t\}] \tag{3.5}$$

The first term of equation 3.5 represents the Rayleigh scattering (frequency ω_0) and the second term the Raman scattering (frequency $\omega_0 - \omega_m$ for the Stokes case and $\omega_0 + \omega_m$ for the anti-Stokes).

The RT Raman spectra of the samples studied (β-Ga_2O_3, GaN, SiC and bulk diamond) were obtained with a Horiba Jobin Yvon HR800 spectrometer, under the incidence of the 442 nm He-Cd (Kimmon IK Series) laser line in the backscattering configuration. A diffraction grating of 600 lines/mm and a 50× objective lens were used. The measurement error is ± 2 cm^{-1}. Figure 3.2 presents a schematic diagram for a Raman system. During a Raman experience, the sample is excited with a laser, then the scattered photons are collected and focused with a lens onto the spectrometer. The Raman-shifted frequencies are detected (usually by a charge coupled device (CCD)) and recorded for analysis [72]. Filters, such as Notch or Edge, are often used to avoid the detection of the Rayleigh scattering.

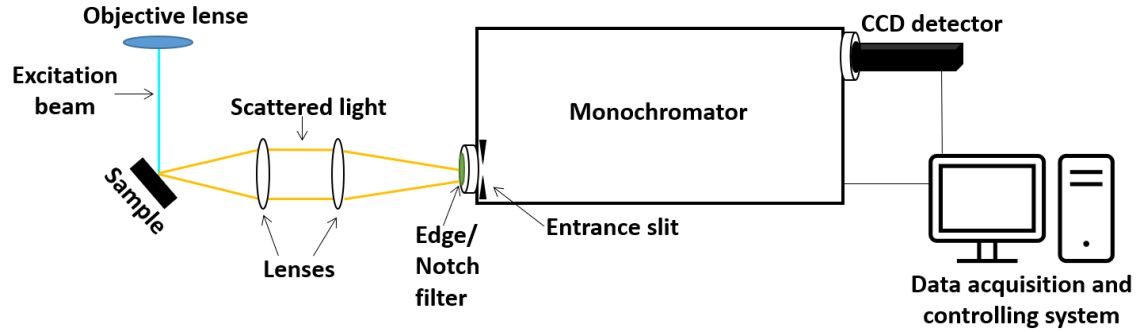

Figure 3.2: Schematic diagram of a Raman measuring system.

3.2 Absorbance and transmittance

Measuring a semiconductor's absorption spectrum is a simple way to determine its electronic band structure. The absorption of light by a material occurs when the incident photon is absorbed by an electron, leaving it in an excited state [36]. When it comes to the case of atoms, their energy level diagram consists on a series of states with discrete energies. However, as already discussed, for semiconductors this diagram is more complex thanks to the formation of bands with their delocalized states [72]. Figure 3.3 presents a schematic diagram of the interband absorption transitions in semiconductors. Here we can see that what makes the distinction between semiconductors is the relative position of the CB minimum and VB maximum in the BZ. As aforementioned, for a direct bandgap, the minimum of the CB and the maximum of the VB are at the same **k** vector, while for an indirect bandgap,

the extremes of the bands appear in different **k** values. For a typical semiconductor, interband optical absorptions are only possible when the photon energy is equal or higher than the bandgap energy [36]. In order to conserve momentum, the electron wave vector can not change significantly during the photon absorption. Consequently, for indirect semiconductors, the transition must involve a phonon to ensure the conservation of momentum. Interband transitions originate a continuous absorption spectrum from the low energy thresold (E_g) to a superior value that is defined by the extreme limits of the involved bands in the process and the corresponding density of states [36, 72].

In addition to the interband transition, other absorption processes may occur in semiconductors since impurities and/or dopants create extra electronic levels in the bandgap [36].

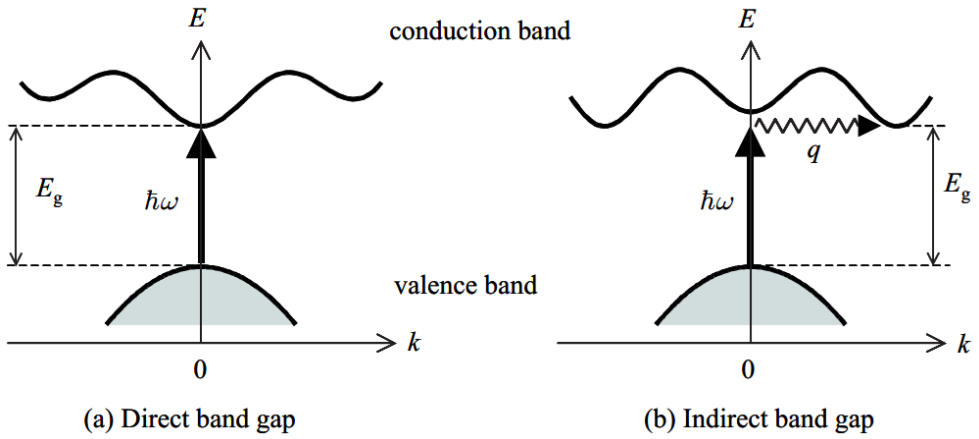

Figure 3.3: Interband absorption transitions in a (a) direct and in an (b) indirect bandgap semiconductor. The vertical arrow represents the photon absorption process and wavy one the emission or absorption of a phonon [72].

RT absorbance/transmittance measurements were performed using a double-beam Shimadzu UV2100 spectrometer in transmission mode for wavelengths from 200 to 800 nm. The spectrometer has deuterium and tungsten-halogen lamps as excitation sources. Figure 4.6 presents a schematic diagram of a double beam spectrometer. In this case, the sample is placed in front of an excitation source that is coupled to a monochromator, which allows the selection of the wavelength range to be scanned. The transmitted signal is analysed taking into consideration the changes regarding the excitation profile and with this one can obtain information on the absorptions that can occur in the sample, and the distribution of electronic states [36].

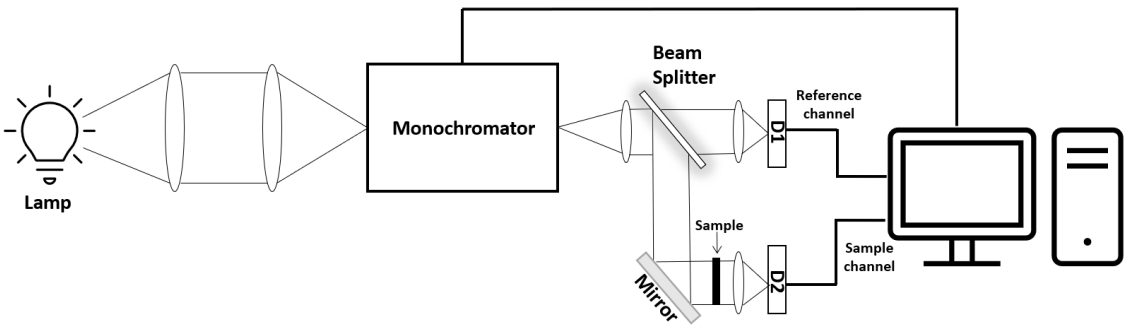

Figure 3.4: Schematic diagram of a double beam spectrometer where D1 and D2 are detectors.

3.3 Luminescence

3.3.1 Theoretical background

The luminescence process in solids, namely in wide energy gap semiconductors, is particularly relevant in the scope of fundamental research and in the recognition of the potential of these materials for various electronic and optoelectronic applications as it allows the characterization of optically active defects. Luminescence is a process related to the energy difference between two electronic states, the emitting state (e) and the ground state (g), and it is observed when a system in the excited state returns to the ground state by emitting photons [72]. We can classify different types of luminescence processes by how the excitation energy is applied, for example: electroluminescence, where an electric field is applied to the material; cathodoluminescence, a high-energy electron beam is used as its excitation source, etc [73]. In this section of the work, we will focus on photoluminescence (PL), where the system is excited with light. This is a very powerful technique for the detection and identification of impurities or defects through the recombination of generated excess carriers in their electronic energy levels [10]. Impurities and defects, whether they are intentional or unintentional introduced into the crystal, can result in the creation of electronic energy levels within the bandgap of the semiconductor. These levels may lead to the appearance of optical transitions at energies lower than the bandgap. Defects and/or impurities like these are called optically active centres [36]. The features of these centres depend on the type of intrinsic defect/dopant and the lattice in which it is incorporated [71].

In a PL experiment, the absorption of photons with an energy equal to or higher than the material's bandgap energy, results in the generation of electron-hole (e-h) pairs, which leads to a non-equilibrium distribution of the e-h pairs. In most situations, the electrons and holes will thermalize among themselves and reach quasi-thermal equilibrium in a shorter time compared to their recombination time, and they may present different quasi-equilibrium distributions. Afterwards, the e-h pairs can recombine radiatively, producing spontaneous emission. Thus it is possible to understand that a luminescence process will involve three main steps: 1) excitation; 2) thermalization; and 3) recombination [74]. Figure 3.5 exemplifies the model of an isolated optical center, composed of a system of only two vibronic (electronic plus vibrational) energy levels, described by the model of the configurational coordinate diagram, Q, which describes the interaction of the defect with the vibrations of the lattice (near neighbouring atoms). In this model, only a single mode of vibration (the symmetrical stretching mode) is considered, in which all the atoms of the cluster of the first near neighbouring atoms move radially in phase (breathing mode). The lattice vibrations is described by the quantum harmonic oscillator model. The vibrations of the ions around their equilibrium positions change the strength of the crystalline field over a given defect in the lattice, affecting the energy of their electronic states. Therefore, the minima of the ground and excited electronic states occur at different values of the coordinate.
In the harmonic approximation, and as illustrated in Figure 3.5, the energy of the electronic states as a function of Q corresponds to a parabola, where Q_0 is equivalent to the equilibrium distance in the fundamental state and Q_0' in the excited state. In the example, and for simplicity purposes, it is assumed the same vibration frequency of the vibrational modes, ω, in both electronic states [71]. The optical transitions are represented by vertical arrows since these steps follow the Franck-Condon principle - the electronic transitions between the two states occur so rapidly that there is no change in the configurational coordinate Q [36]. The parabolic lines in Figure 3.5 represent potential energy of the ground ($U_g(Q) = 1/2k_gQ_0^2$) and the excited ($U_e(Q) = 1/2k_e(Q_{0'} - Q_0)^2 + U_0$) levels, whereas the horizontal lines over each curve represent the vibrational energy states [71]. At low temperatures, an optically active

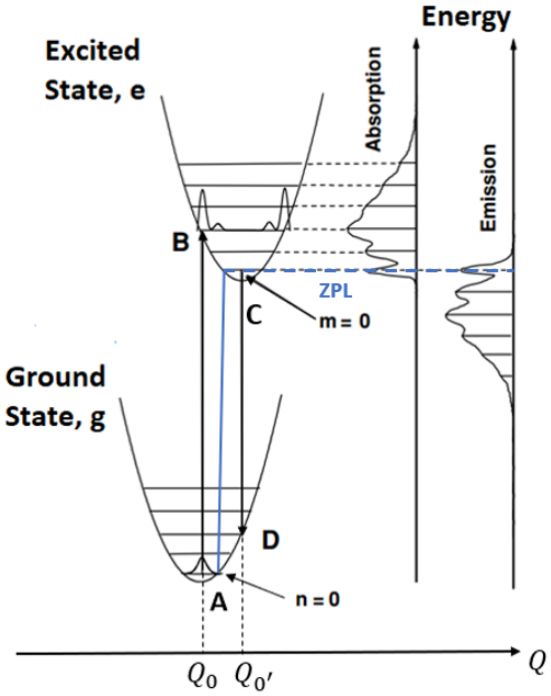

Figure 3.5: Configurational coordinate diagram model for the ground state (g) and the first electronic excited state (e). The absorption and emission band profiles are drawn based on the $n = 0 \rightarrow m$ (absorption) and $m = 0 \rightarrow n$ (emission) relative transition probabilities, being n and m the vibrational levels of the ground and excited states, respectively. Q_0 and $Q_{0'}$ correspond to the equilibrium distance in the ground and excited electronic states, respectively. The ZPL is also present in blue. Adapted from [71].

center lies in lowest vibrational state of the electronic ground level.

Exciting an electron from its fundamental to an excited state corresponds to the vertical absorption A $\rightarrow$ B in Figure 3.5. The probability of the optical transition between the lowest vibrational level (n=0) of the ground electronic state and the vibrational level m=m of the excited state is proportional to the square of the product $< e(Q)|r|g(Q) >< \chi_m|\chi_0 >$ (allowed by assuming the validity of the Franck Condon principle), where $e.r$ corresponds to the electric dipole moment and χ to the quantum harmonic oscillator vibrational wave functions. The first factor is called an electronic transition matrix element and is independent of vibrational levels, while the second factor corresponds to the vibrational overlap integral. One can say that a way to formulate the Franck-Condon principle is to postulate that the overall transition matrix element is proportional to the overlap integral of the vibrational wavefunctions of the ground and excited levels. The transition n=0 to m=0 is called zero phonon line (ZPL) and does not involve vibrations, with the latter altering the spectral shape but not the intensity of the transition provided by the electronic transition matrix element [71]. Following the absorption, the system relaxes by radiationless processes to its lowest vibrational level (C), losing some of its energy in the form of phonons. Luminescence happens when the electron returns to the ground state (D) and it is followed by another relaxation process in order for the electron to reach the level with the minimum potential (A), with emitting phonons. In the C $\rightarrow$ D transition, a photon is emitted, with lower energy than the energy absorbed in A $\rightarrow$ B [36]. This is a consequence of the relaxation process and the difference between the absorption and emission maxima is called Stokes shift (ΔE_{Stokes}). To quantify the electron-

phonon coupling, one uses the Huang-Rhys factor, S, which is given by $\Delta E_{Stokes} = 2S\omega\hbar$ (assuming that the vibrational frequency for the ground and excited state is the same). As mentioned, the transitions that occur without the assistance of phonons are designated by ZPL and their intensity is stronger for S values smaller than 1. As S increases, the intensity of such lines decreases and vibrational side bands appear [71].

In a typical PL experience, the excitation source (with a given excitation wavelength corresponding to a region where the sample absorbs) illuminates the sample and one measures how the PL intensity varies as a function of the wavelength.

PLE is a complementing spectroscopy technique to PL and it is particularly useful to assess the preferential pathways for excitation of the optical centres [36]. In this case, the exciting energy is continuously changed while the emission monochromator is set at a fixed wavelength (chosen by its user), which is the emission wavelength one wants to monitor. The user then checks which radiative paths are most favourable to obtain the specific luminescence intended to study. The observed features in the PLE spectra offer information on the processes involved in the excitation of a specific transition and allow the identification of the optimum conditions for its excitation [75]. In addition, this technique is also complementary to absorption measurements.

3.3.2 Experimental setup

The PL and PLE measurements were performed using a Fluorolog-3 from Horiba Scientific. A continuous 450 W Xe lamp was utilized as excitation source, coupled to a Gemini 180 excitation monochromator with a diffraction grating of 1200 lines/mm and a focal distance of 180 mm. The emission light from the interaction with the sample, is directed to an iHR550 scanning emission monochromator with a diffraction grating of 1200 lines/mm and a focal distance of 550 mm. The detector used was an R928P photomultiplier tube (PMT), and all measurements were acquired using the front face acquisition geometry, with an angle of $\sim 30^{o}$ between the excitation and the collection. All measured spectra were corrected to the optics of the system and to the detector response. Figure 3.6 presents a schematic diagram of the system. In the PLE case, the same equipment was used, in which the scanning monochromator was kept fixed at the maximum emission and the excitation monochromator was scanned for smaller wavelengths.

A dispersive system SPEX 1074 *Czerny-Turner* monochromator with a diffracting grating of 1200 lines/mm and a focal distance of 1 m was used to obtain both RT, excitation dependent and temperature dependent PL data. Three different excitation sources were used in these studies, a He-Cd laser line with a wavelength of 325 nm, and two solid-state laser lines with wavelengths at 405 nm and 532 nm. The samples were firmly fixed in a cold finger of a closed-cycle helium cryostat under vacuum conditions ($\sim 10^{-5}$ mbar). The vacuum was achieved using a vacuum system composed of two pumps: a primary (rotative) and a secondary (turbomolecular). This allowed the temperature to reach a minimum of approximately 14 K. The temperature dependence study was performed by raising the temperature from 14 K to RT, using a heating resistance placed closely to the cold finger and controlled by a temperature controller coupled to a thermo-couple. The detector used was a electrical and water cooled Hamamatsu R928 PMT. The PL excitation density dependence study was conducted using neutral density filters. All measured spectra were corrected to the optics of the system and to the detector response. Figure 3.7 presents a schematic diagram of the system used for the PL measurements. A set of lenses focus the emitted light from the sample into the monochromator's entrance slits. After passing through the dispersive system, the light is collected by the PMT detector and processed by an analysis software [36].

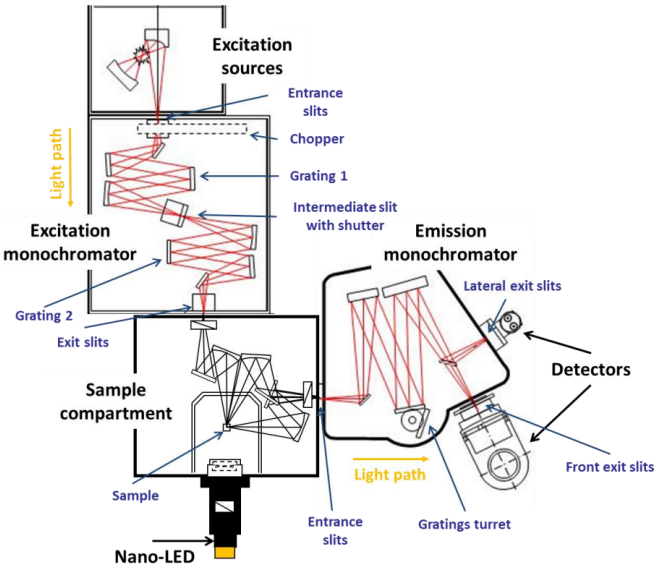

Figure 3.6: Schematic diagram of the Fluorolog-3 system used for RT PL and PLE measurements [36].

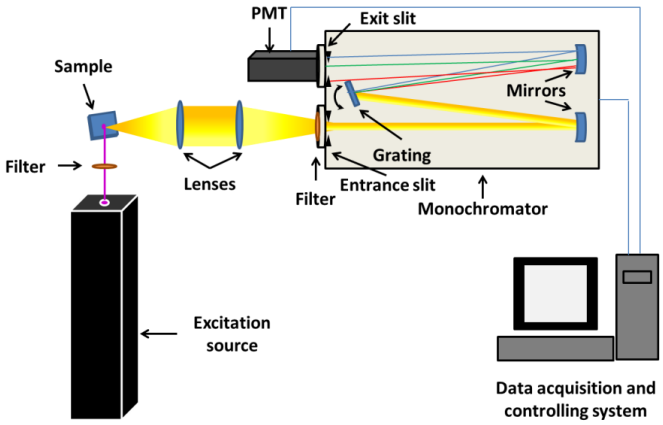

Figure 3.7: Schematic diagram of the SPEX 1074 *Czerny-Turner* monochromator system used for PL measurements [36].

3.4 Samples description

The description of the WBS and UWBS bulk, homo and heterostructures that were characterized in this work is presented in Table 3.1. The β-Ga_2O_3, GaN and 4H-SiC films were all grown by metal organic chemical vapour deposition (MOCVD). Figure 3.8 presents a schematic of the SiC homostructure with the type, thickness and carrier density for each layer.

Table 3.1: WBS and UWBS semiconductor's characteristics.

Sample	**Description**
Ga_2O_3	n-type (Si doped) Ga_2O_3 (200 nm) on semi-insulating (Mg doped) Ga_2O_3 substrate (500 μm)
GaN	unintentionally doped GaN on sapphire
SiC (1) Homostructure, Fig. 3.8	commercial CREE n-type 4H-SiC
Diamond (Bulk 1)	Bulk diamond (transparent)
Diamond (Bulk 2)	Bulk diamond (dark yellow)

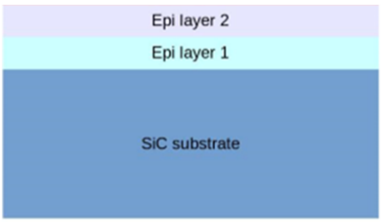

(a)

	Type	Thickness (µm)	Carrier concentration (cm^{-3})
Substrate	4n/n	300	--
Epi1	n	0.5	1×10^{18}
Epi2	n	10	0.66×10^{16}

(b)

Figure 3.8: (a) Schematic representation of the 4H-SiC homostructure; (b) type, thickness and carrier density for each layer.

Chapter 4

Results and discussion

4.1 Optical characterization

One of the most important aspects in the manufacture and design of optical and electrical devices is the need for high-quality epitaxial thin films. A direct way to improve the quality of not only the material properties of the films but also the devices themselves is to avoid undesirable impurities and minimizing structural imperfections [10]. All of these impurities are lattice defects, decreasing the crystal quality. Hence the importance of studying defects in semiconductors - if there is a clear understanding of their impact on the material, it becomes possible to align strategies to avoid and/or control them and achieve reproducibility with higher performance devices.

4.1.1 Raman spectroscopy

The structural properties of all the samples were evaluated by Raman spectroscopy, and the identification of the vibrational modes characteristic of each of the materials was done. Several spectra were measured for each sample and no significant differences were observed, which attests to their homogeneity. The following figures in this section are representative spectra of each of the samples.

As stated previously, the optical modes expected for β-Ga_2O_3 are $\Gamma_{opt} = 10A_g + 4A_u + 5B_g + 8B_u$, where A_g and B_g are active in Raman [33]. The experimental Raman spectrum obtained for the sample studied in this work, without analysis of its polarization, is shown in Figure 4.1. By comparing the frequencies of these modes with the ones found in the literature it was possible to identify the observed modes (Table 4.1).

Table 4.1: Energy location of all the vibrational modes observed in Raman for the β-Ga_2O_3 sample and the comparison with the ones found on literature.

Phonon mode	Observed modes in the present work (cm^{-1})	Experimental modes in reference [76] (cm^{-1})
B_g	146.8	144.8
A_g	171.4	169.9
A_g	203.4	200.2
A_g	323.9	320.0
A_g	348.6	346.6
A_g	419.9	416.2
A_g, B_g	479.0	474.9
A_g	631.6	630.0
A_g	658.7	658.3
A_g	769.4	766.7

The modes with Raman shifts below 200 cm^{-1} reflect the translation and libration motions

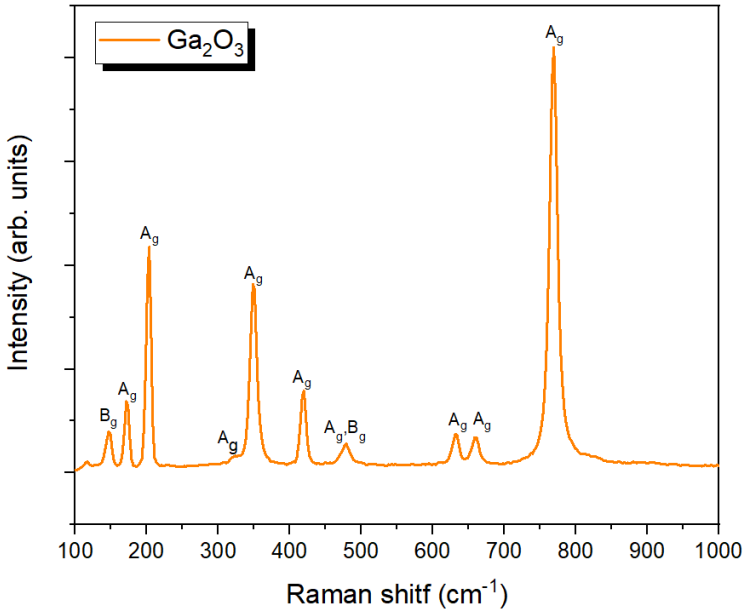

Figure 4.1: Raman spectrum of the β-Ga_2O_3 sample for backscattering geometry under excitation of 442 nm at RT.

of the tetrahedra chains. The following group of modes, with shifts from 300 to ~470 cm^{-1} are related to the translation of the octahedra and the deformation of the tetrahedra. The final group of modes with shifts above ~470 cm^{-1} reflect the stretching and bending of the tetrahedra [77].

Although 15 Raman modes were expected, not all where observed in our results. Considering the measurement error, half of the Raman shift's values have an error greater than the measurement error. This could mean that the sample may have stress effects between the n-type layer that was grown on the semi-insulating substrate of β-Ga_2O_3. Additionally, one has to also consider the penetration depth of the laser into the sample surface. According to Zongwei Xu *et al.* [78], this can be calculated by the following Equation 4.1.

$$d_p = \frac{2.3}{2\alpha} \tag{4.1}$$

where d_p is the penetration depth and α the absorption coefficient. This coefficient depends on the material and the laser line utilized. Therefore, considering the absorption coefficient reported by Hassanien *et al.* [79] the estimate for the penetration depth for the β-Ga_2O_3 sample with the 442 nm laser line was 115 μm, meaning that the probed Raman arises either from the n-type doped epilayer and semi insulating substrate.

The modes observed for GaN (Figure 4.2) and 4H-SiC at RT (Figure 4.3 and Table 4.2) were identified according to the data reported in the literature [80, 81].

As previously discussed, some vibrational modes of GaN are polarized, which allows one to determine the orientation of the film being studied. For the WZ structure, the Raman tensor has both diagonal and off-diagonal components present for the E_2 phonon mode. However, for the A_1 phonon mode, the Raman tensor only has diagonal components, meaning that this mode can only be observed when the incident and scattered light have parallel polarization [82]. Since both these modes were observed, this means that the film is Ga-faced and its polar plane is {0001}. The A_1(LO) mode was observed at 737.4 cm^{-1}. Furthermore, a substrate signal can also be observed at 419.9 cm^{-1} in Figure 4.2, in accordance with the

estimated penetration depth of the laser line (0.330 μm) considering the GaN coefficient absorption reported by Muth *et al.* [83], corresponding to the vibrational mode of sapphire. Even though the thickness of the GaN layer is unknown, one can say it is smaller than the penetration depth. As there is a large lattice mismatch between the layer and substrate between the lattice parameters of the two materials ($\sim$ 16 %), this may result in a high defect density, which can affect the GaN properties [37]. Indeed, most GaN properties depend on the growth method and the quality of the samples [36]. In this sense, Raman spectroscopy can be a great tool to examine film quality and monitor residual stress. The electrical and optical properties of epitaxial films are greatly influenced by residual stress due to the mismatch of lattice constants and the thermal expansion coefficients of the substrate and epitaxial film [84]. Such phenomena can be reflected in the peak position of the observed Raman modes. For instance, the position of the E_2 Raman mode of the GaN layer can be shifted due to stress: the upshift of the peak frequency corresponds to a compressive stress, while the downshift corresponds to a tensile one [85]. Kisielowski *et al.* [86] concluded that a biaxial stress of 1 GPa would shift the E_2 phonon mode (with respect to the unstrained GaN) by 4.2$\pm$0.3 cm^{-1}. The stress-free standard value for the position of E_2 is 567.6 cm^{-1} at RT [80]. A close inspection to the data acquired in this work revealed that the energy position of the E_2 phonon mode was at 572.5 cm^{-1} which indicated that the film presents a compressive stress of $\sim$ 1.17 GPa, estimated taking into account the work reported by Kisielowski *et al.* [86].

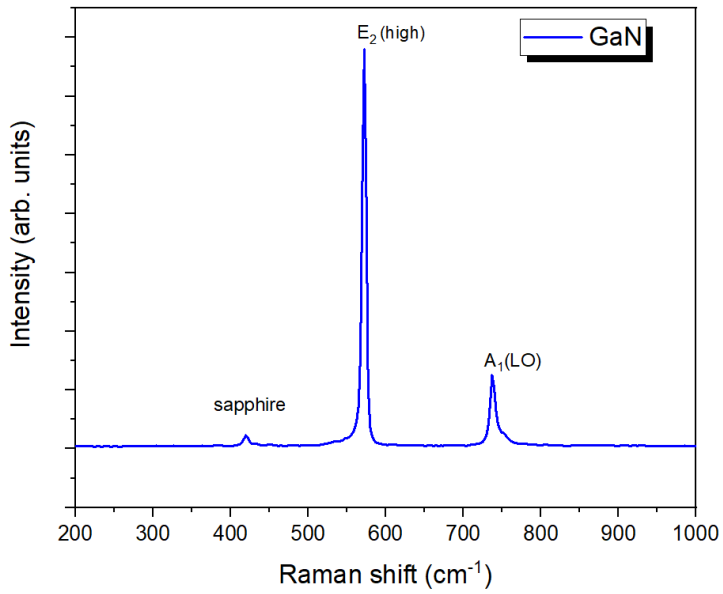

Figure 4.2: Raman spectrum of the GaN sample for backscattering geometry under excitation of 442 nm at RT.

For 4H-SiC, 8 Raman modes were expected yet the measured spectrum only presented 5. Indeed, the peak positions obtained experimentally in this work appear considerably shifted regarding the ones reported for bulk 4H-SiC [81, 87], with a shift higher than limit of the experimental error. Similarly to the case of β-Ga_2O_3, we also have to consider the laser penetration depth to understand if the modes we measured are from the epilayers or the substrate. Although a value for the absorption coefficient for 4H-SiC when excited with 442 nm was not found in the literature, Sridhara *et al.* [88] present the square root of the absorption coefficient as a function of wavelength for 4H-SiC and with this an estimate was made for the absorption coefficient. In this way, the penetration depth calculated was 2875 μm, which means this that, the signal measured comes from all the sample, including

the two epilayers and substrate. The sample studied is a homostructure, thus stress effects cannot be discarded. The Raman's shift observed for the TO modes are generally associated with stress in 4H-SiC [89]. Considering that the only TO mode observed was E_2, the stress effects will be studied through this mode. The stress free value of this mode is 777 cm^{-1}. The atomic displacement of the E_2 mode is perpendicular to the c axis, making it sensitive to stress perpendicular to this axis [90]. Even though it is usually reported that the Raman shift decreases as the tensile stress increases in TO modes [90,91], there is not an established correlation between the frequency shift and the stress. For example, Sugiyama *et al.* [91] reported a relationship between the frequency shift and the positive tensile stress on (0001) as -1.96 GPa/cm^{-1}. Sugie and Uchida [90] reported that the frequency shift in E_2 for an isotropic biaxial stress in the c plane was -323 MPa/cm^{-1}. Since a clear relationship between the effect of stress on Raman shift has not yet been established, as in the case of GaN, it is not possible to conclude on what stress the film is actually under. Furthermore, the E_2 mode position obtained in this work is higher than the defined stress free, which may indicate that the film is under compressive stress.

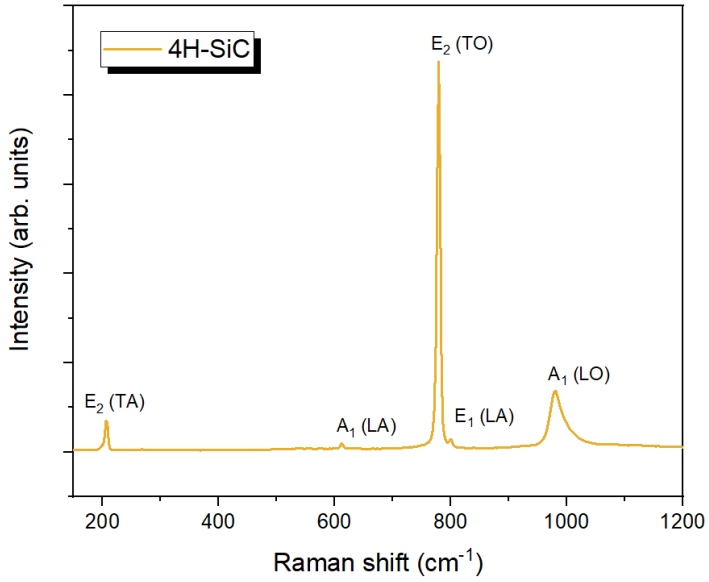

Figure 4.3: Raman spectrum of the 4H-SiC sample for backscattering geometry under excitation of 442 nm at RT.

Table 4.2: Energy location of all the vibrational modes observed in Raman for the 4H-SiC sample and the comparison with the ones found on literature.

Phonon mode	Observed modes (cm^{-1})	Experimental modes (cm^{-1}) [81,87]
E_2 (TA)	205.8	202.2
A_1 (LA)	611.9	608.6
E_2 (TO)	779.2	777.0
E_1 (LA)	801.4	797.0
A_1 (LO)	981.1	985.0

The identification of the vibrational modes by Raman spectroscopy of bulk diamond is somewhat a simple procedure - there is only one vibrational mode (T_{2g}), thus there is only a sharp Raman line at about 1332 cm^{-1} [92]. Figure 4.4 presents the RT Raman spectrum of a bulk diamond (1) sample with the identification of the respective mode.

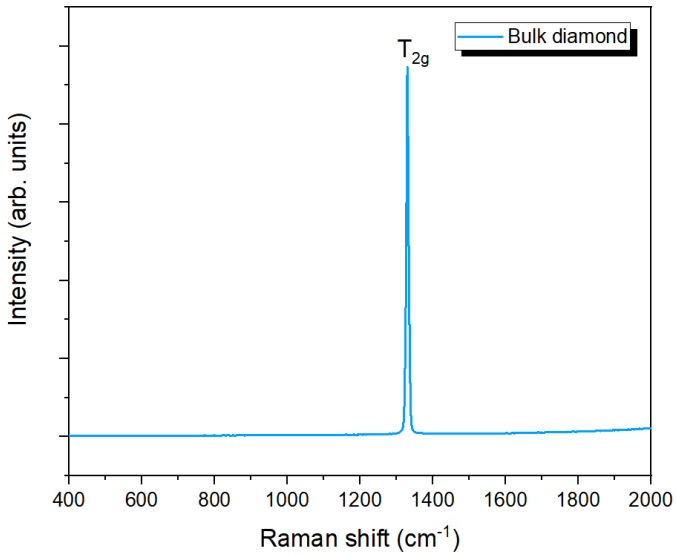

Figure 4.4: Raman spectrum of the diamond Bulk 1 sample for backscattering geometry under excitation of 442 nm at RT.

4.1.2 RT transmission of WBS and UWBS grown by epitaxy

Figure 4.5 displays the RT transmission spectra of the WBS and UWBS studied in this work. The onset of the transmission is 258 nm (∼4.81 eV) for β-Ga_2O_3, 360 nm (∼3.4 eV) for GaN, and 357 nm (∼3.47 eV) for 4H-SiC. With the exception of 4H-SiC, the obtained values agree well with the energies reported in the literature that were mentioned in the second chapter (Table 2.1).

In the GaN spectrum an interference pattern is observed, which indicates that the GaN layer has parallel faces.

Although gallium oxide is consensually a direct semiconductor (E_g = 4.87 eV) [29], the transmission spectrum of β-Ga_2O_3 shows two main absorption bands at 4.81 eV and 4.53 eV (273 nm) corresponding to the material bandgap when light is polarized parallel to the b and c-axis, respectively [93].

In the case of the 4H-SiC sample, two pronounced defect-related absorption bands were observed at 463 nm (∼2.68 eV) and 567 nm (∼2.19 eV). The high bandgap energy obtained experimentally for 4H-SiC (compared to the expected value in literature of 3.3 eV [25]) is most likely caused by an overlap of absorption transitions to the nearest indirect minima of the CB, as also reported by W. M. Klahold *et al.* [94]. The sharp absorption edge located at 3.47 eV (357 nm) for 4H-SiC is considered to be caused by the absorption from the top levels of the VB to the bottom levels of the CB. The below bandgap absorption bands have been reported in 4H-SiC doped with N impurity [95], which is known to give rise to a shallow donor level 45-65 meV below the CB minimum [96]. These optical resonances, also known as Biedermann bands [97], have been attributed to transitions from the CB minimum to higher CB (inter CB transitions), in accordance with the scheme depicted in Figure 4.6. To account

for the peak position and full width at half maximum (FWHM) of the absorption bands, the authors consider the role of the selection rules, as well as, the possibility of a mixture of states (including the N levels) to be involved in the transitions. The broadening of the band increases with increasing N concentration [95].

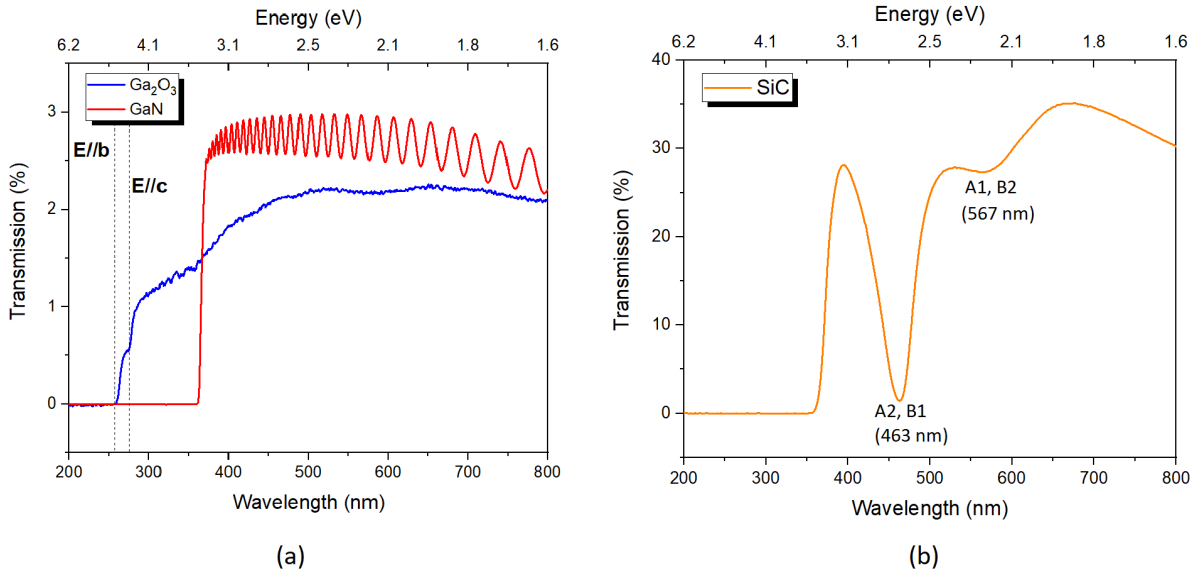

Figure 4.5: RT transmission of the (a) β-Ga_2O_3, GaN and (b) 4H-SiC samples.

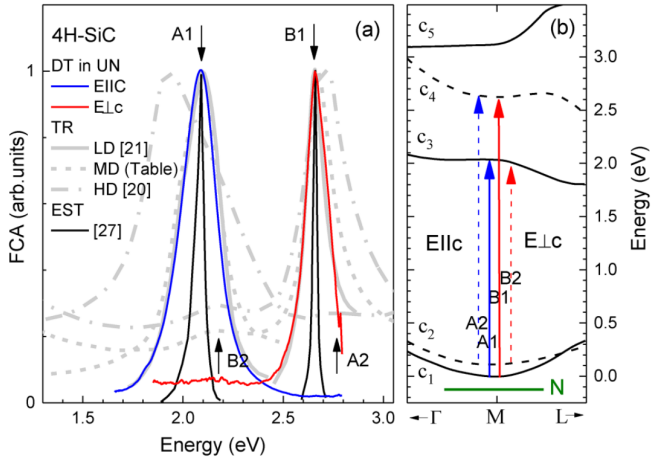

Figure 4.6: (a) Normalized free carrier absorption spectra in excited undoped 4H-SiC (red and blue curves) in comparison to the optical transmission data in n-type 4H-SiC with different dopings (grey curves) and theoretical estimates (black curves). (b) Electronic structure of the CB in 4H-SiC with the allowed transitions for the two light polarizations (red and blue arrows) [95].

4.1.3 PL/PLE analysis

Photoluminescence is a great tool for the optical characterization of semiconductors - it allows the detection and identification of distinct optically active defects as a result of their recombination mechanisms [10]. In this section the results from the PL/PLE analysis conducted in this work are discussed. All samples were excited by using photons with energy equal or higher than the bandgap energy. In some specific cases sub bandgap photons were used as excitation sources.

4.1.3.1 Gallium oxide

For any new semiconductor technology, conductivity control through doping and mitigation of trap states is essential to achieve device applications. Point defects are imperfections that occur in a specific site in a crystal lattice. They can be divided into two categories: a) intrinsic defects, such as vacancies (missing atoms), interstitials (displaced atoms from their regular crystal site), and antisites (the original atom is replaced by another host atom in the crystal); and b) extrinsic defects involving impurity atoms. If an atom is deliberately introduced into the crystal lattice, then it is called a dopant [9]. As previously discussed in chapter 2, β-Ga_2O_3 presents a low-symmetry crystal structure, which leads to a complex optoelectronic behaviour - its optical properties are anisotropic and its typical emission spectrum do not exhibit near-band-edge (NBE) emission [98]. Rather, the emission spectra may show UV luminescence (UVL), blue luminesnce (BL) and green luminescence (GL) bands [10]. In Figure 4.7 ((a) and (b)) the RT PLE and PL spectra of the analysed β-Ga_2O_3 sample are presented.

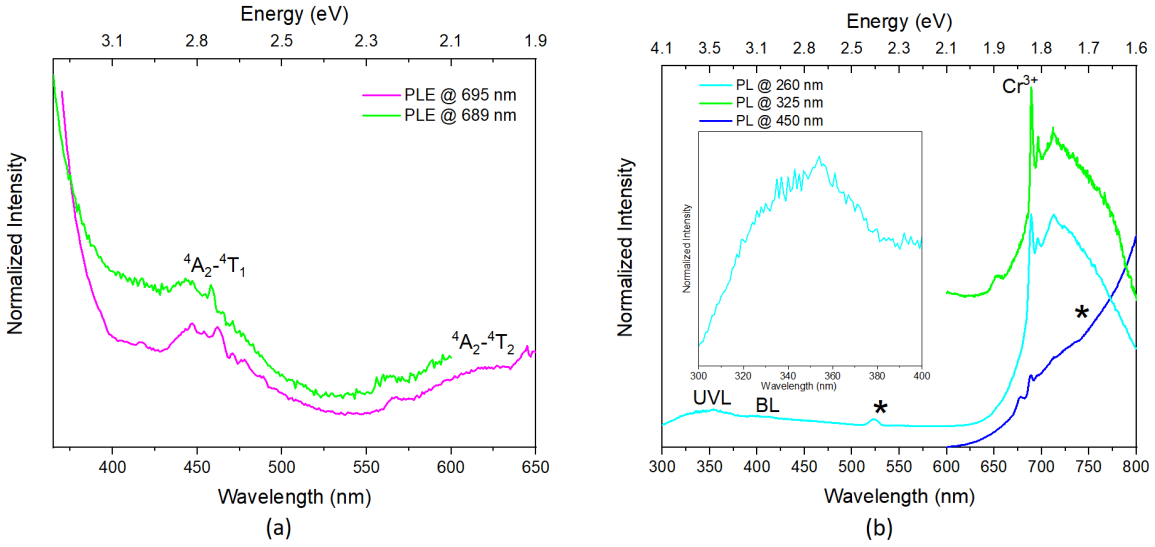

Figure 4.7: (a) RT PLE spectra and (b) RT PL spectra of the β-Ga_2O_3 sample. The spectra were shifted vertically for clarity. The * indicates a second order from the excitation.

The RT PL spectrum obtained with above band gap excitation, shows the UVL band (inset in Figure 4.7 (b)) centred around 354 nm. The UVL band has been attributed to the recombination of free electrons and self-trapped holes (STH) or self-trapped excitons (STE), and it is commonly identified as impurity independent [10]. The electrons in the CB of β-Ga_2O_3 are delocalized, however the holes are self-trapped states - the holes are trapped in a local electric field induced by displacements of oxygen atoms [10]. As for the STE, what happens is

that an exciton can be self trapped by its own lattice distortion field if there is a strong local deformation of the crystal lattice [99]. However, there is still much debate in the scientific community about the nature and model of recombination of this emission. In fact, more recent works reveal that the energy position of this emission depends on the conductive or semi-isolating character of the samples and, consequently, on the impurities present [100]. It should also be mentioned that in the most used growth methods (Czochralski, edge fine growth and chemical vapour deposition (CVD)) the presence of Si contaminants (shallow donor associated with the n-type conductivity of the samples), Ir (from the crucibles used), Fe and Cr (due to the purity of the precursors) is frequent [10, 101]. Moreover, the studied sample is composed by a n-type Si-doped (activation energy of 46.5 meV below the CB [102]) and a Mg-doped semi-insulating (Mg is a deep acceptor with activation energy of 1.0 - 1.5 eV above the VB [103]) substrate. Consequently, for the moment, it cannot be excluded that the UVL band could be due to other types of defects/impurities.

The BL and GL bands are usually attributed to donor-acceptor pair (DAP) transitions [101, 104]. For the BL case, the DAP transitions may involve deep donors and acceptors. Some authors, considered as possible donors for undoped β-Ga_2O_3 O vacancies (V_O) and interstitial Ga (G_i) and possible acceptors Ga vacancies (V_{Ga}) and V_O-V_{Ga} complexes [10]. However, as for the case of the UVL the chemical species involved on the defect that originates the BL is still a matter of controversy. In the studied sample, a BL is observed around 400 nm (∼3.10 eV). The GL is not observed. Additionally, in Figure 4.7 (b), a red luminescence (RL) band with sharp ZPLs at around 688.5 nm (∼1.801 eV) and 695.8 nm (∼1.782 eV) followed by a vibronic structure, is observed. The red emission can be attributed to the intraionic $^4T_2$, $^2E \rightarrow {}^4A_2$ transitions in the Cr^{3+} ions ($3d^3$ configuration) sitting in the distorted octahedral G(II) sites [105–109]. Figure 4.8 presents a schematic energy diagram of Cr^{3+} in β-Ga_2O_3 [107].

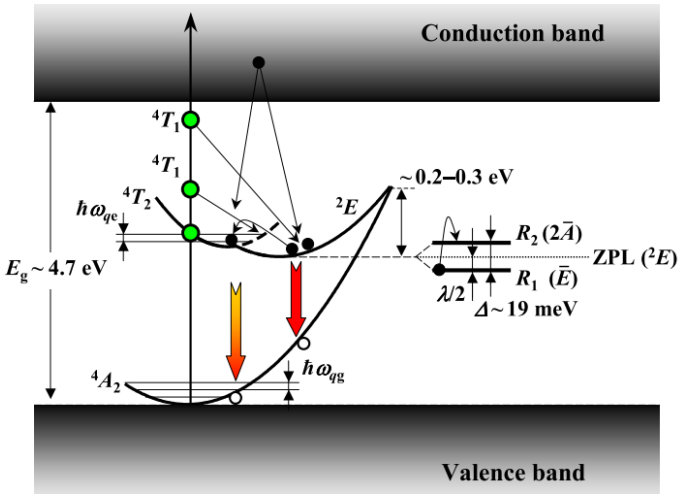

Figure 4.8: Schematic energy diagram of the Cr^{3+} ion in monoclinic gallium oxide [107].

The RT PLE spectra monitored at the Cr^{3+} emission, is shown in Figure 4.7 (a). Two noticed excitation bands peaked at around 600 nm (∼2.1 eV) and 460 nm (∼2.7 eV) are observed, corresponding to the intraionic Cr^{3+} absorption from the ground state, $^4A_2$, to the $^4T_2$ and $^4T_1$ excited states, respectively [107].

Cooling down the sample temperature at 14 K allows the identification of features in optical spectra that are not observable at RT. Figure 4.9 shows a comparison between the Cr^{3+} emission observed at RT and at 14 K under selective excitation. Three main excitation

wavelengths were used: 325 nm, 405 nm and 532 nm. While the first one corresponds to a photon absorption nearby the β-Ga_2O_3 band edge, the two last correspond to nearly photon energies that preferentially excite the Cr^{3+} ions, as indicated by the PLE spectra. With the excitation conditions used it is possible to clearly discern the presence of ZPLs called R-lines, centred at 688.9 nm (∼1.8 eV) (R2) and 696.2 nm (∼1.781 eV) (R1) that correspond to the $^2E \rightarrow {}^4A_2$ transition of Cr^{3+}, overlapped with a broad asymmetric band due to the $^4T_2 \rightarrow {}^4A_2$ transition [107]. It can be seen that at low temperature the intensity of the R lines is much higher than that of the vibronic band, and that increasing temperature favours a decrease in the PL intensity of the lines at the expense of increasing the band intensity and the population of the higher excited energy state, $^4T_2$. As mentioned, Figure 4.8 presents a schematic energy diagram of the Cr^{3+} ion in β-Ga_2O_3 based on the configurational-coordinate model, where $^4A_2$ is the ground state and ^2E, $^4T_2$, and $^4T_1$ are excited states. Under intermediate crystal field the ^2E state corresponds to the lowest energy excited state [107, 108, 110, 111] and the two R lines result from the splitting of the ^2E state due to the action of the trigonal crystal field (the Cr ions in Ga(II) are in a distorted octahedral position) and spin-orbit interaction [107, 108, 110, 111]. The splitting of the ^2E state in the studied sample was found to be 19 meV in agreement with the value reported in literature [107].

An additional comment should be made regarding the origin of the collected emission: whether it comes from the epilayer or the substrate. Since the epilayer is n-type, it would be expected to observe a higher intensity of UVL emission than from Cr^{3+}. Indeed, it has been reported in the literature that the intensity of UVL emission increases with the concentration of shallow donors in n-type samples [10]. However, this was not observed experimentally (see Figure 4.6 (b)) and, consequently, it is likely that the most collected emission comes from the β-Ga_2O_3 semi-insulating substrate. In this case, impurities such as Fe and Cr act as compensators of shallow donors, with Cr^{3+} emission being dominant.

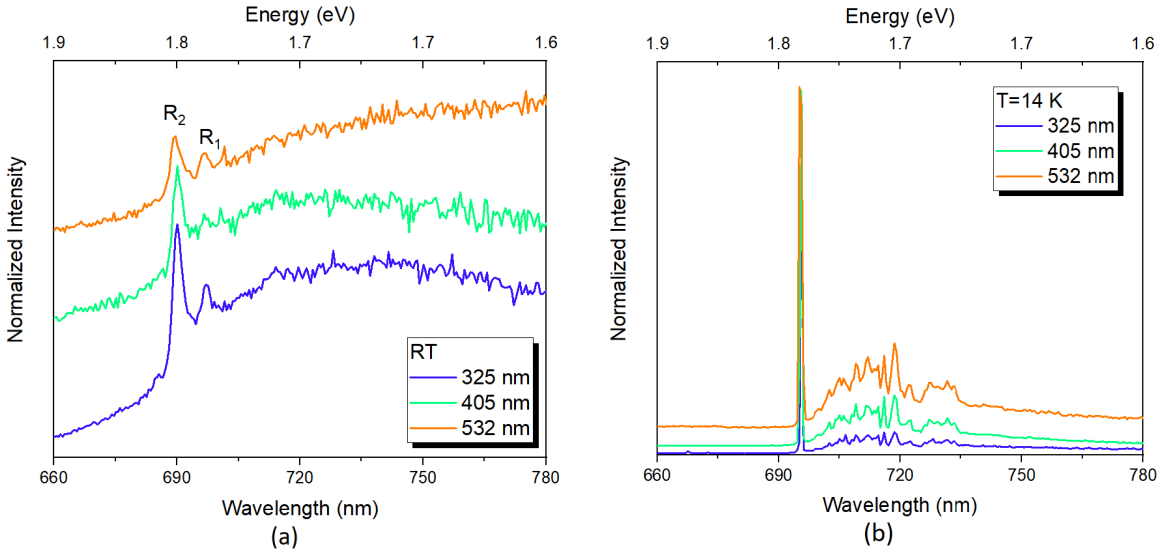

Figure 4.9: PL spectra obtained under the excitation of 325 nm, 405 nm, and 532 nm laser lines, acquired at (a) RT and (b) 14 K for the β-Ga_2O_3 sample. The spectra were shifted vertically for clarity.

4.1.3.2 Gallium nitride

Even though GaN is a highly interesting material for several electronic and optoelectronic applications, it contains several structural and point defects that affect the performance and reliability of devices [112]. So it is extremely important to study these defects to achieve further improvements in GaN-based devices.

One of the most widely observed emission bands in GaN PL spectra is a broad yellow luminescence (YL1) band peaked at ∼2.2 eV with reports of this band dating back to the 1970's [113]. The origin of this YL1 band is still debatable, however, recent works indicate that the band is due to a carbon in a an nitrogen site (C_N), which is in accordance with earlier works [114]. In 1980, Ogino and Aoki [114] attributed the YL1 band to a complex defect consisting of a Ga vacancy (V_{Ga}) and a C atom in the site of the Ga nearest neighbour. This configuration is improbable because both V_{Ga} and C_N act as acceptors, which makes them unlikely to bind [115]. Since carbon has a similar atomic radius to N, it is expected to preferentially occupy the N lattice site. Early first-principles calculations based on DFT predicted the C_N to be a shallow acceptor. However, more reliable first-principles calculations using the Heyd-Scuseria-Ernzerhof (HSE) functional show that the C_N acceptor level is deep (0.9-1.1 eV above the VB maximum) [116]. It is important to note that despite the extensive studies on the YL1, the question of its origin maintains. In Figure 4.10 a predominant broad YL1 band is observed at RT in the studied sample, with band-to-band excitation. The emission is modulated by interference fringes. As seen in the same figure by the PLE spectra, when the PL is monitored at the the band maxima, the YL1 luminescence is preferentially excited by above GaN bandgap photon energies. A noticed peak is identified at 363 nm that corresponds to the GaN bandgap.

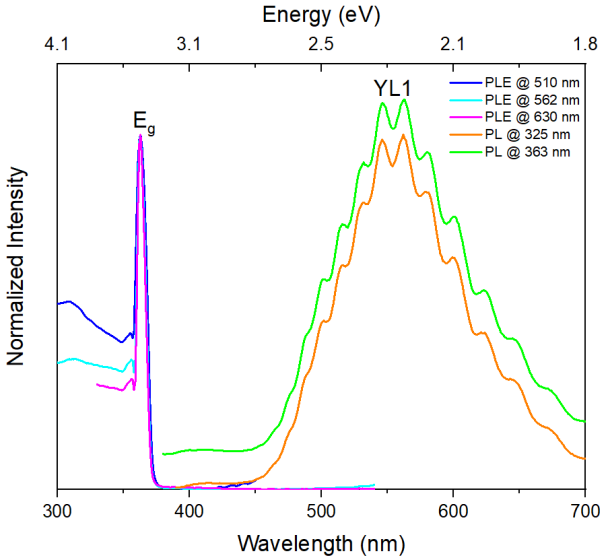

Figure 4.10: RT PL and PLE spectra of the GaN sample. The PL spectra were vertically shifted for clarity.

At low temperatures, Figure 4.11, in addition to the YL1 band, NBE emission due to free excitons (FX) and donor bound exciton (DX) transitions and their phonon replicas were also observed. The FX is an elementary excitation, considered as the first excited state of a pure crystal, and is generated upon band-to-band excitation, where an electron at the maximum of the VB is promoted to the minimum of the CB. These carriers attracted themselves by electrostatic interaction, forming an *e-h* pair with a behaviour similar to the H

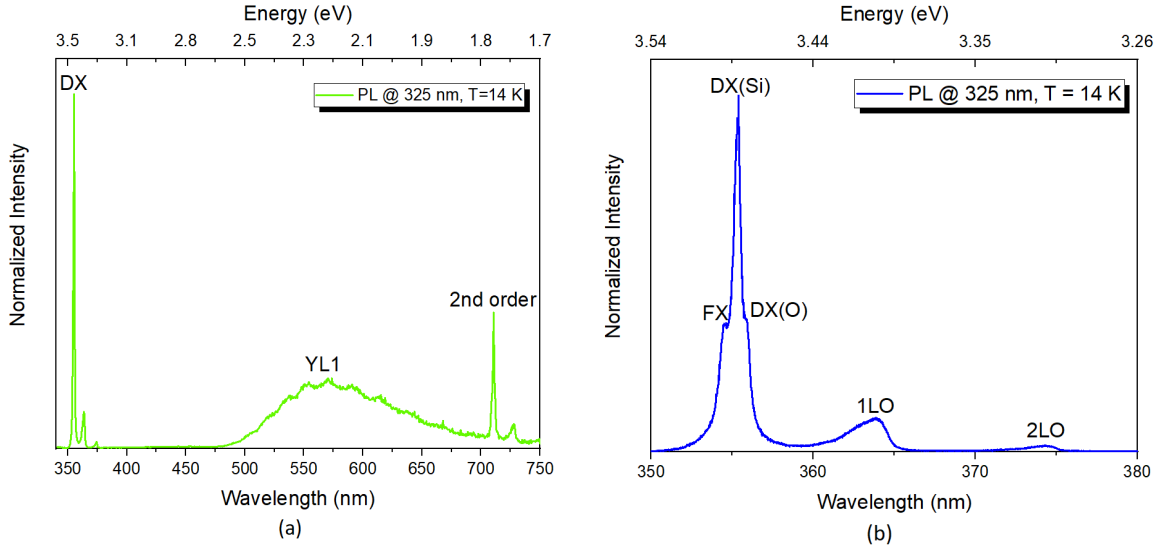

Figure 4.11: 14 K PL spectra obtained with the excitation of 325 nm laser line, acquired (a) in the UV-Vis-NIR range and (b) a high-resolution PL spectrum acquired in the NBE region.

atom embedded in the crystal lattice. The FX energy levels are modulated by the dielectric constant of the material and the FX recombination occurs at photon energies close to the bandgap given by $hf = E_g(T) - E_x$, where E_x corresponds to the FX exciton binding energy (in the case of GaN, E_x is close to 25 meV). In GaN pure samples, the fundamental optical transitions that occur at the Γ point of the first BZ involves the FX recombination considering a hole of the three uppermost VB states, designated as A, B and C [36]. As discussed previously in chapter 2, the crystal field and spin-orbit interactions split the VB into three bands - A is the top valence band (Γ_9 symmetry), followed by B (Γ_7 symmetry) and the lowest being C (Γ_7 symmetry) [117]. Figure 4.12 presents a schematic diagram for this splitting. The FX that arise from these bands are labelled FX_A, FX_B and FX_C, respectively.

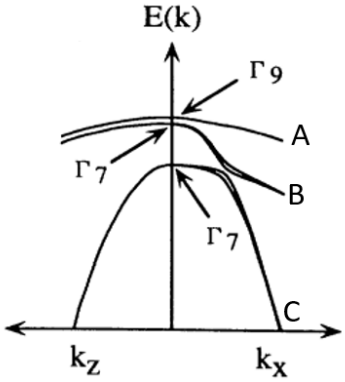

Figure 4.12: Schematic VB structure near the Γ point of WZ GaN. Adapted from [118].

The sample studied here is an epilayer and, in this case, the spectral position is highly dependent on the strain state of the sample [36]. With the information from the Raman spectra it was concluded that the film presented a biaxial strain, which most likely will modify the spectral position of the FX, if present. DX transitions are also frequently present

in n-type GaN and they have relevant importance in the characterization of materials since they act as optical signatures of the presence of impurities. The recombination energy of a bound exciton occurs at lower energies than the FX being given by $hf' = hf(FX_A) - E_{loc}$, with E_{loc} being the bound exciton localization energy known as Hayne's rule $E_{loc=}0.2_D$, with E_D the donor binding energy [119]. The DX in GaN is commonly associated with the recombination of an FX_A with a neutral O donor on the N site (O_N) or a neutral Si donor on the Ga site (Si_{Ga}). Both impurities are shallow donors in GaN layers with binding energies (determined from the two electron transitions) of around 33.2 meV and 30 meV below the CB minimum, for O and Si, respectively [117]. Figure 4.11 (a) and (b) evidence the strongest NBE of the studied GaN layer at 14 K. The higher energy transition in the GaN layer occurs at 354 nm (∼3.503 eV) which is higher than the FX_A value reported for unstrained GaN (ca. 356.5 nm (∼ 3.478 eV), confirming that the studied sample is under compressive strain [120]. For the studied sample and considering E_x = 25 meV, a bandgap energy of 3.528 eV is estimated for the material at 14 K. At lower energies than the FX recombination, a line at 355.4 nm (∼3.489 eV) with a shoulder at 355.8 nm (∼3.485 eV) can be clearly discerned, and are assigned to the common shallow donors in GaN (Si and O, respectively). From the spectra binding energies of the 14 meV and 18 meV were determined for Si and O, respectively (the accuracy of this calculation is lower than the one determined by two electron transitions). Furthermore, at lower energies 1LO (ca. 92 meV) and 2LO phonon replicas of the FX and DX transitions are observed.

At low temperatures, DAP recombinations involving the shallow donors and acceptors (when present) are also commonly seen in the GaN emission spectra near by 3.27 eV [112]. In the studied sample, no DAP transition was observed as expected for a non intentionally doped layer (Table 3.1) that exhibits intrinsic n-type behaviour due to Si and O impurities.

As it was possible to identify all the features mentioned above, one can say that although there is strain in the film, it still presents a good optical quality, as identified by the NBE/YL1 intensity ratio at low temperatures.

4.1.3.3 Silicon carbide

One of the difficulties in studying and characterizing SiC is the fact that there are over 200 polytypes, all of which have different physical properties. So, before beginning its study it is of great importance to clarify the structure in question [121]. The structure of the sample in this work, 4H-SiC, was confirmed by both the transmission (Figure 4.5 (b)) and the Raman spectra (Figure 4.3) present in the previous sections.

In Figure 4.13 ((a) and (b)) the normalized RT PLE and PL spectra of the 4H-SiC sample is shown. Under low excitation conditions (Xe lamp coupled to a monochromator), the RT PL obtained upon band-to-band excitation reveals the presence of two broad luminescence bands in the blue and green spectral regions, peaked ca. 416 nm (∼3.0 eV; BL) and 520 nm (∼2.4 eV; GL). When monitored at the emission band's maxima, the PLE spectra evidence a noticed excitation band at ca. 3.5 eV, corresponding to the material bandgap, in agreement with the measured transmission spectrum. Moreover, the BL and GL bands are also excited by below bandgap excitation, as revealed by the overlap of excitation bands in the near band edge region. Particularly, for the case of the structured BL, the emission is favoured for excitation with 376 nm (∼3.3 eV).

The BL was previously reported in N doped 4H-SiC samples and is attributed to a DAP transition between the shallow N donor and the Al acceptor [122–124]. As mentioned, the N donor gives rise to two shallow levels nearby 45-65 meV and 105-125 meV when placed in hexagonal and cubic sites, respectively [96]. Moreover, besides N, common impurities in 4H-SiC are Al, the most common acceptor with an energy level placed ∼200 meV above the

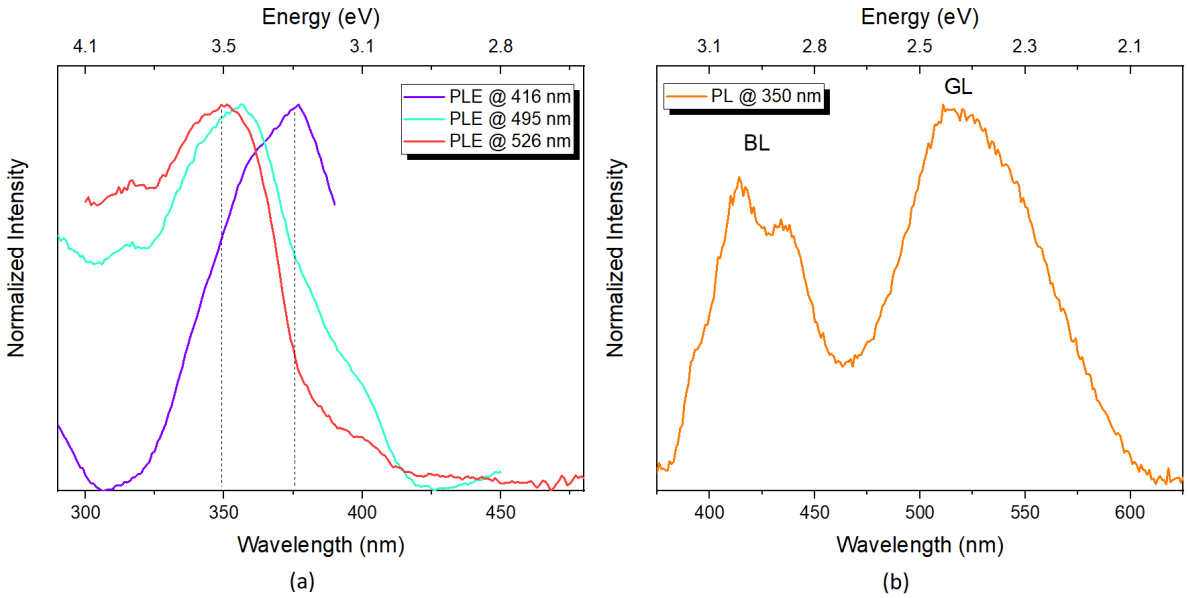

Figure 4.13: RT (a) PLE spectra and (b) PL spectrum of the 4H-SiC sample under low excitation density conditions (Xe-lamp).

VB [125], and B [123, 126]. B introduces two energy levels in the bandgap: a) a shallow level, with an ionization energy of ∼0.3 eV, and b) a deep level, the so-called D centre, with ionization energy of approximately 0.58-0.68 eV above the top of the VB [126]. An isolated B impurity residing at the Si site (B_{Si}) is responsible for the shallow level. The D centre, in current understanding, consists of a complex comprising a B_{Si} with an adjacent carbon vacancy (V_C) [127]. These impurities can coexist in 4H-SiC samples [124]. As mentioned, besides the BL band, an asymmetric GL is observed, with the used excitation conditions. The GL was found to be observed in B-doped and co-doped samples [123,124,126,128,129] and was attributed to a DAP recombination and an electron-acceptor (e-A) transition involving the N shallow donor and the B acceptor. The peak position of the GL is known to be dependent on the Si/C ratio used during the growth process, showing a low-energy shift for higher Si/C contents and high B concentrations [124].

Figure 4.14 (a) shows the 14 K PL spectra of the studied 4H-SiC obtained with above band gap excitation using the 325 nm line of an He-Cd laser (high excitation density conditions). Noticed changes can be observed when a comparison is made with the results of Figure 4.13.

At 14 K, the main PL recombination is dominated by a broad emission band peaked at 659 nm (∼1.9 eV), hereafter designated by RL. Additionally, on the high energy side, new features are observed nearby the BL, which also evidence a slightly different spectral shape, which may indicate an overlap of emitting centres in the same region. A magnification of the high energy spectral region is shown in Figure 4.14 (b) where the typical Q_0 and P_0 lines due to the recombination excitons bound to neutral N donors at hexagonal and cubic sites and phonon replicas are observed [130, 131]. This is a strong evidence that we need to consider the two shallow N levels for the explanation of the recombination processes.

Moreover, to get further insight into the nature of the broad GL band, a PL excitation density study was conducted, Figure 4.14 (c). To do so, neutral density filters were used. These filters evenly reduce the transmission of the excitation light and are typically defined by their optical density (OD), which describes the amount of energy blocked by the filter [132]. The percent transmission (T) of the filter is given by Equation 4.2 and the information

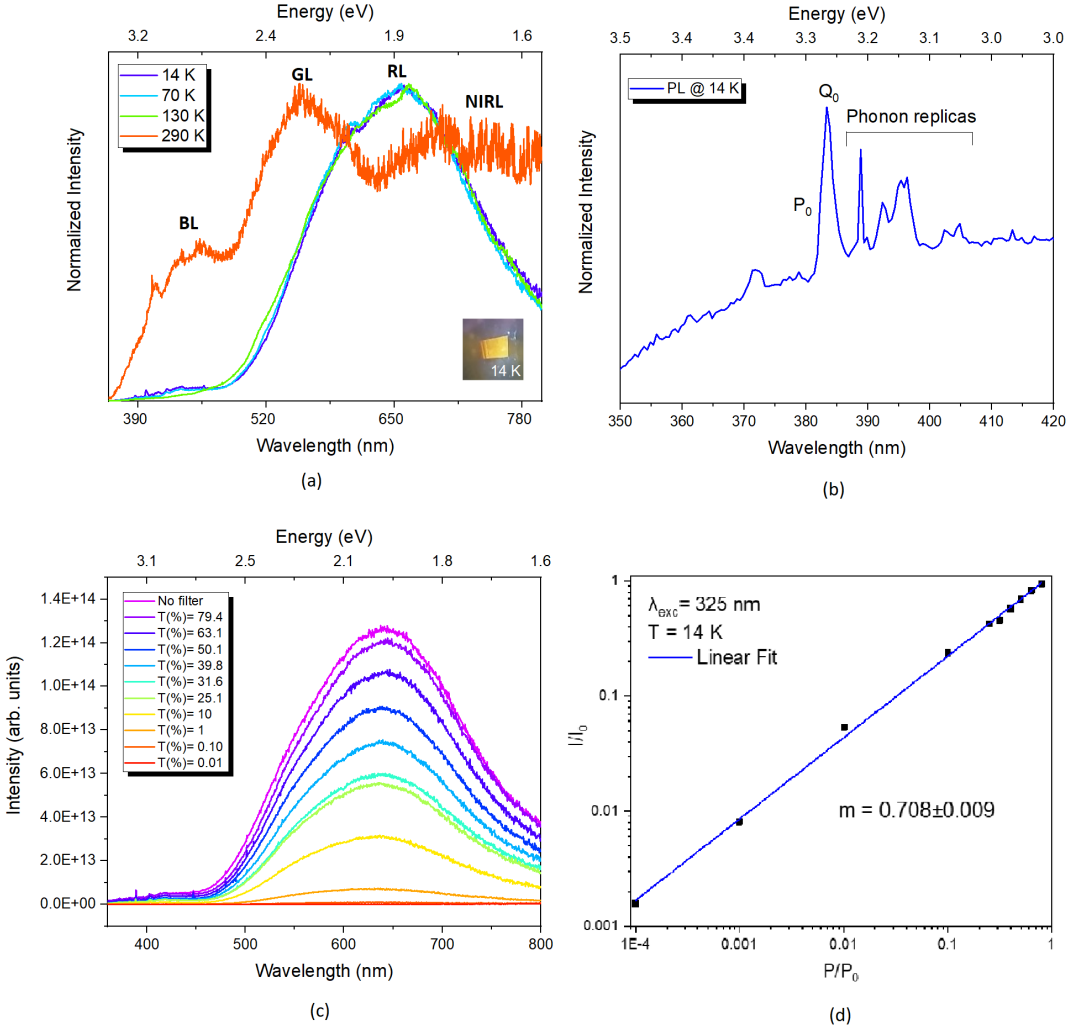

Figure 4.14: (a) PL spectra obtained under the excitation of 325 nm laser line for different temperatures and (b) close up of the high-energy region of the 14 K spectrum of the 4H-SiC sample. (c) Excitation density-dependent PL spectra acquired with a 325 nm laser excitation. (d) *Log(I/I$_0$)-log(P/P$_0$)* plot for the broad bands presented in (c).

regarding the filters used is present in Figure 4.14 (c).

$$T(\%) = 10^{-OD} \cdot 100\% \tag{4.2}$$

We can see from Figure 4.14 (c) that the PL intensity decreases and that the broad band maximum does not shift with decreasing excitation density. Schmidt *et al.* [133] reported that the PL intensity of the emission can be fitted to a power law, $I \; \alpha \; P^m$, where I is the luminescence intensity, P the excitation power and m is the value of the slope in a *log-log* representation of I and P. Figure 4.14 (d) presents the *log(I/I$_0$)-log(P/P$_0$)* representation along with the corresponding linear fit. The analysis showed a slope of 0.708 ± 0.009 for the excitation density study performed at 14 K, which, according to the same authors [133], indicates that the nature of the transitions either involves free-to-bound carrier or DAP recombination. Nevertheless, a deeper analysis of the nature of the RL should be conducted. In fact, the large FWHM of the RL suggests that the emission could be due to an overlap

of emitting centres in the same spectral region. Temperature dependent PL studies (shown normalized in Figure 4.14 (a)) allow us to observe that no shifts in the RL peak position occur with increasing temperature up to 130 K, meaning that no e-A transition is detected at this temperature. At RT, the GL is dominant and a near infrared luminescence (NIRL) band peaked ca. 726 nm (∼1.7 eV) can also be identified. As such, a possible explanation for the RL is that it results from the superposition of the GL and NIRL. If this is the case, NIR emission should be favoured at low temperatures compared to the GL. Considering the observed emissions and known impurities present in the 4H-SiC, a possible schematic diagram of the observed transitions is depicted in Figure 4.15, for which, with the information from the experimental data, we cannot conclude what is the nature of the defect that causes the NIRL. However, since the GL is a DAP recombination and the result of the excitation density study over the entire band evidenced that it behaves like a DAP emission, it is likely that the 1.7 eV NIRL band also presents a DAP nature, eventually involving B impurities. As stated in the conclusions and future work, more studies are needed to confirm these hypotheses.

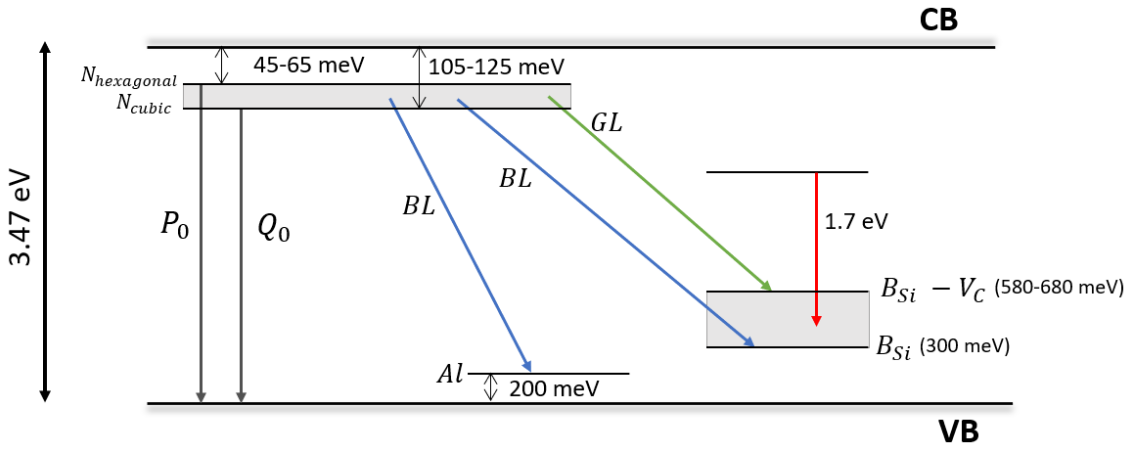

Figure 4.15: Schematic diagram of the proposed phenomena occuring in 4H-SiC under above bandgap excitation.

4.1.3.4 Diamond

In order to assess the optical active centres in diamond the samples, PL and PLE spectra were acquired under different excitation conditions.

Figure 4.16 (a) presents the RT PL and PLE spectra of diamond Bulk 1 and one can immediately see the almost perfect mirror symmetry of the excitation and emission features around the ZPL of the N3 centre. This centre is frequently observed in type Ia diamond and consists of three N atoms surrounding a vacancy (Figure 4.16 (b)). The emission of this center is characterized by a ZPL at 415 nm, accompanied by two prominent sidebands with phonons of ∼ 90 and 165 meV energy [134]. The PLE spectrum monitored at the PL band maximum of the N3 centre shows a strong excitation band peaked at 380 nm and an excitation band centred at 330 nm due to the N2 centre, which is of vibronic origin and is non-luminescent [134, 135]. This means that the N3 centre is excited directly through its excited states and by the N2 centre.

The low temperature PL spectra of the Bulk 1 diamond is shown in Figure 4.17. A magnification of the ZPL and the vibronic bands is depicted in Figure 4.17 (b). The blue emission of the sample could be clearly seen by the naked eye when the sample was under excitation by the 325 nm laser line (Figure 4.17 (a)).

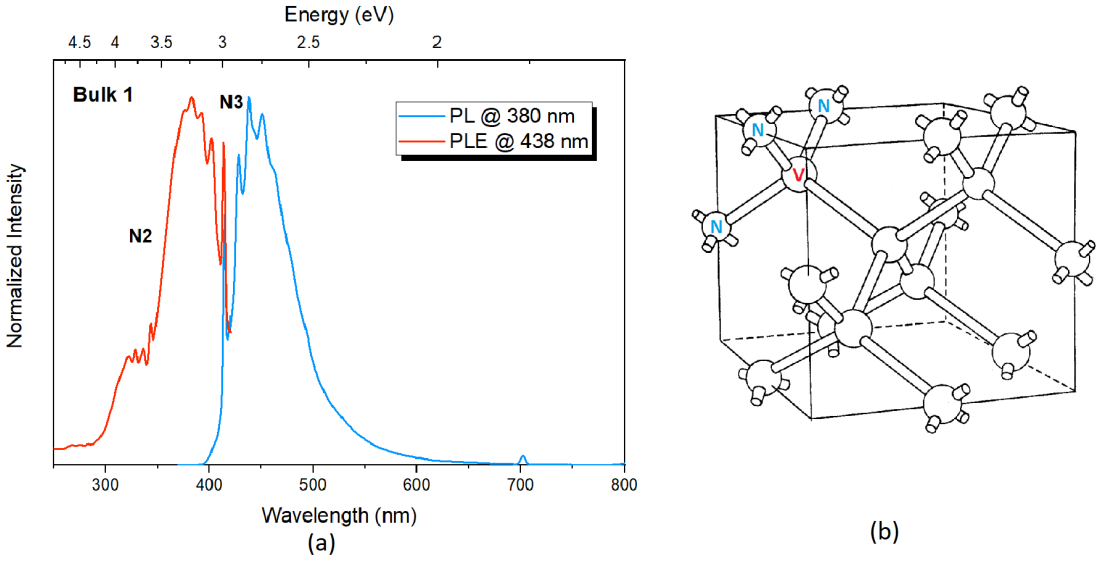

Figure 4.16: (a) RT PL and PLE spectra obtained for a Bulk 1 diamond sample; (b) schematic diagram of the N3 defect, where V corresponds to the C vacancy and N the three N atoms. Adapted from [136].

To further explore the optically active centres in diamond, an extra bulk diamond sample (Bulk 2, Table 3.1) was analysed. In Figure 4.18 (a) the RT PL and PLE spectra of the Bulk 2 sample are represented. Similarly to what was observed for the Bulk 1 diamond, here one can also see a symmetry of the excitation and emission features. However, in this case the features are around the ZPL of the H3 centre. The emission maximum was around 520 nm (∼2.385 eV). The H3 center consists of two substitutional N atoms (A aggregates) separated by a vacancy (N-V-N structure with C_{2v} symmetry) [137] as depicted in 4.18 (b). This centre has its ZPL at 503.2 nm (∼2.464 eV) [135] and corresponds to the transition between the ground state (A_1) and the first excited state (B_1). A small shoulder can also be observed in the PL spectra at ∼573 nm (∼2.164 eV), and it corresponds to NV^0 [54, 138]. The NV centre consists of a N atom adjacent to a vacancy oriented along the direction [111] with C_{3v} symmetry [138]. A schematic diagram of this centre can be seen in Figure 4.18 (b). The subscript 0 indicates that defect is in its neutral charge state [54]. This centre is typically observed in CVD diamonds. It can be formed during the actual synthesis process, of ion implantation and annealing, or by radiation damage and annealing [138]. The formation of a high concentration of holes and their diffusion during annealing enhances their capture by substitutional impurities of N, leading to the formation of the NV centre [138].

With the used excitation conditions, no further luminescence defects were observed at RT.

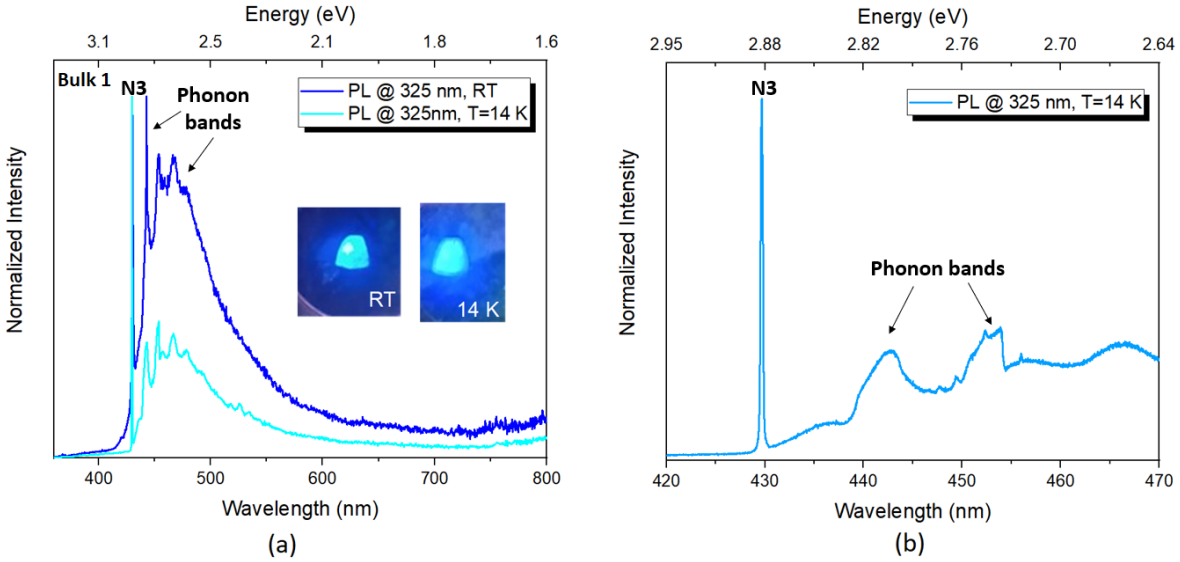

Figure 4.17: PL spectra obtained under the excitation of 325 nm laser line, acquired at (a) RT and 14 K; The visual appearance of the sample's emission at RT and 14 K is also presented. (b) a high-resolution PL spectrum obtained at 14 K.

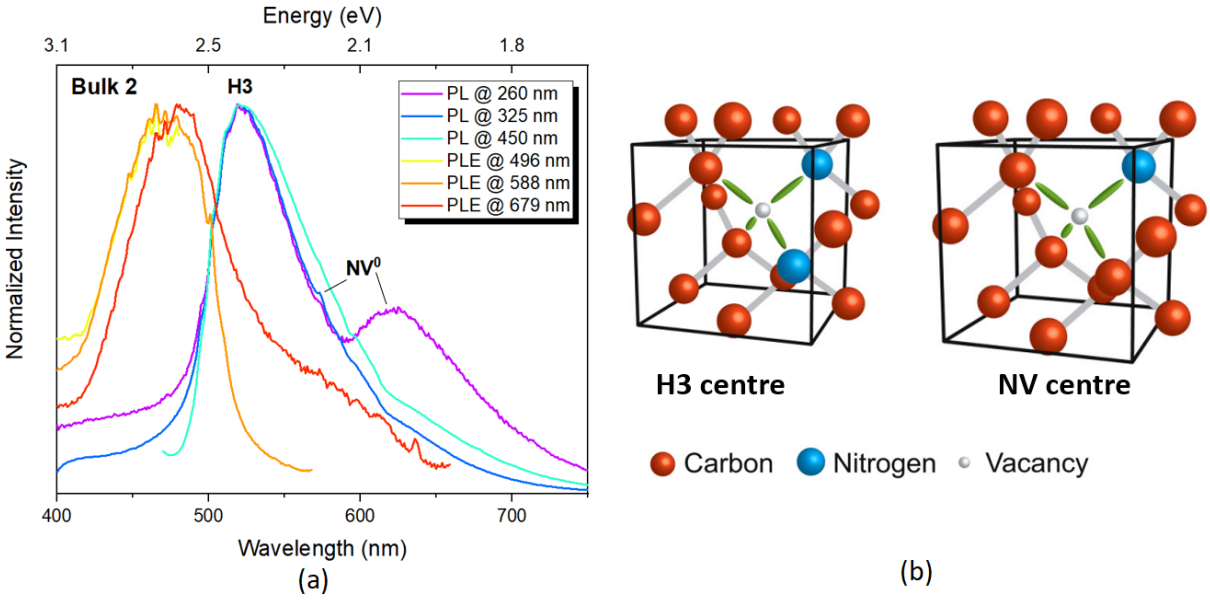

Figure 4.18: (a) RT PL and PLE spectra obtained for a Bulk 2 diamond sample; (b) schematic diagram of the H3 and NV centres. Adapted from [139].

Chapter 5

Conclusions and future work

Nowadays, semiconductors play a great part in our lives and with growing energy demands, comes the demand for better electronic and optoelectronic devices. WBS and UWBS are great competitors for the current technology, with β-Ga_2O_3, GaN, 4H-SiC and diamond being of particular interest.

With this work, it was possible to broaden and deepen the theoretical knowledge acquired throughout the years of studying semiconductor physics in different curricular units, as well as to obtain hands-on experience with different spectroscopy techniques.

As mentioned several times along this work, characterizing optically active defects in semiconductors is immensely important - a better understanding of these defects will allow the achievement of more efficient electronic and optoelectronic devices.

In this work, bulk, homo and heterostructures of different WBS (GaN and 4H-SiC) and UWBS (β-Ga_2O_3 and diamond) were optically characterized by Raman, transmittance and PL/PLE with the purpose to identify the samples structural quality and evaluate the presence of optically active defects.

With Raman spectroscopy, we were able to identify 11 of the 15 Raman modes that were expected for β-Ga_2O_3. However, half of these present a significant error, so even though stress effects could not be discarded, it was not possible to identify the type of stress present on the film. Two absorption bands (4.81 eV and 4.53 eV) were observed in the transmission spectra of β-Ga_2O_3 due to anisotropic effects. These bands correspond to the material bandgap when light is parallel to the b and c-axis, respectively. Firstly, RT PL and PLE measurements were acquired for the sample. The PL spectra presented UVL, BL and RL band. Although the UVL band is typically attributed to the recombination of STH and STE, for the moment, one cannot exclude the possibility that this band may be due to other types of defects/impurities, as for instance Si dopant that was introduced for the n-type doping of the layer. The BL band is mostly attributed to DAP transitions. In the studied sample its low intensity hampers a definitive assignment. Finally, the RL band was associated to the presence of Cr^{3+} impurities in the sample, likely incorporated in the semi-insulating substrate. This defect was also monitored by PLE and the intraionic absorption from the ground state ($^4A_2$) to the excited states ($^4T_2$ and $^4T_1$) was observed. The low temperature PL spectra further allowed the identification of the features of the Cr^{3+} emission. The two characteristic R lines of this emission due to the ^2E to the $^4A_2$ transition were clearly seen and, as expected, the R_1 and R_2 lines are separated by 19 meV.

In contrast to the Raman analysis of β-Ga_2O_3, the analysis on GaN allowed the identification of a compressive stress ($\sim$1.17 GPa) between the GaN layer and the sapphire substrate. Furthermore, it was possible to conclude that the sample was Ga-face with polar plane {0001}. Additionally to the GaN Raman modes, a substrate signal was identified allowing estimate a layer thickness lower than 300 nm. The transmission of the GaN film confirmed a direct 3.40 eV bandgap energy and an interference pattern was also observed, indicating that the GaN layer has parallel faces. The YL1 band was found to be the dominant emission in the PL spectra of GaN. This band is preferentially excited with above the GaN bandgap photon

energies. The origin of this band remains debatable, with current works reporting that it consists of a C_N. Lowering the temperature, a NBE emission due to FX and DX transitions was clearly identified. The DX transitions were assigned to the common shallow donors Si (∼3.489 eV) and O (∼3.485 eV). Their binding energy was calculated: 14 meV for Si and 18 meV for O. Phonon replicas of the FX and DX transitions were also observed at lower energies in the 14 K PL spectra.

The 4H-SiC sample, as can be seen throughout this work, was the most explored. In addition to the Raman, transmittance, PL/PLE analysis, a low temperature excitation density study was also carried out. The objective of this was to understand the emission mechanisms of the defect band present in the low temperature spectrum at ca. 660 nm. Under low excitation conditions, the RT PL spectrum presented two luminescence bands - a BL and a GL band. When the emission maxima were monitored by PLE, an excitation band is visible at 3.47 eV, confirming the transmission result for the bandgap energy. Moreover the emission bands are preferentially excited upon above bandgap photon energies and energies close to the bandgap. The BL band is attributed to a DAP transition between the shallow N donor and an Al acceptor, both being common impurities in 4H-SiC. The GL band is commonly observed in B doped and co-doped samples and is typically attributed to a DAP recombination or an e-A transition involving an N shallow donor and B as an acceptor. B is another common impurity and it introduces two energy levels (a shallow and a deep level). The position of the GL band peak is dependent on the Si/C ratio utilized in the growth process. At low temperatures and high excitation density conditions, the PL spectrum presents a quite different behaviour: it is dominated by a broad RL band. Here, the low temperature excitation density study allowed to conclude that the overall band behaves as DAP or an e-A transition. No shift in the band peak was observed as the temperature was increased (at least up to 130 K). The full width at half maximum suggested that this emission may be an overlap of emitting centres in the same spectral region (GL+NIRL). Besides this band, in the high energy region, two lines were discerned. Both are due to the recombination of excitons bounded to N donors into hexagonal and cubic sites.

Two different bulk diamond samples were analysed, a transparent (Bulk 1) and a dark yellow (Bulk 2) diamond. Raman, RT PL/PLE and low temperature PL were performed for Bulk 1, while only RT PL/PLE was done on Bulk 2. As expected, the sample presented the T_{2g} phonon mode line at 1332 cm^{-1}. For the Bulk 1 sample, the presence of the N3 and the N2 centres was verified. As for the Bulk 2 sample, two different centres were observed: the H3 and the NV^0.

The work developed allowed us to identify that these semiconductor materials have optically active defects, and these give rise to shallow and deep electronic levels. Some of these defects are deliberately introduced through doping, others are intrinsic to the growth processes and may be native or contaminants. In order to infer about the models of recombination of these and other defects it is intended, in a near future, to perform complementary analyses that include the study of: 1) optical absorption in the infrared region; 2) dependence with the temperature and with the excitation density of the intensity of the emission bands and 3) time resolved luminescence and decay measurements. In parallel with this analysis, electron microscopy studies, other structural characterization studies and electrical measurements in the layers will also be conducted. The aggregation of the information from these measurements is crucial for the fundamental knowledge of WBS and UWBS and their optimization for the development of electronic and optoelectronic devices.

Bibliography

[1] E. Braun and S. Macdonald. *Revolution in Miniature*. Cambridge University Press, 2003.

[2] G. Pearson and W. Brattain. History of semiconductor research. *Proceedings of the IRE*, 43:1794–1806, 1955.

[3] W. Grylls Adams and R. Day. V. the action of light on selenium. *Proceedings of the Royal Society of London*, 25:113–117, 1877.

[4] E. Hall. On a new action of the magnet on electric currents. *American Journal of Mathematics*, 2, 1879.

[5] P. R. Morris. *A History of the World Semi-Conductor Industry*. Institute of Electrical Engineers, 2000.

[6] M. Liao, B. Shen, and Z. Wang. Preface. In *Ultra-wide Bandgap Semiconductor Materials*. Elsevier Science, 2009.

[7] Y. Yao, L. Lyle, J. Rokholt, S. Okur, G. Tompa, T. Salagaj, N. Sbrockey, R. Davis, and L. Porter. Growth and characterization of $\alpha-$, $\beta-$, and ε-Ga_2O_3 epitaxial layers on sapphire. *ECS Transactions*, 80:191, 2017.

[8] J. Y. Tsao, S. Chowdhury, M. Hollis, D. Jena, and N. Johnson *et al.* Ultrawide-bandgap semiconductors: research opportunities and challenges. *Advanced Electronic Materials*, 4:1600501, 2017.

[9] S. Pearton, J. Yang, P. Cary, F. Ren, J. Kim, M. Tadjer, and M. Mastro. A review of Ga_2O_3 materials, processing, and devices. *Applied Physics Reviews*, 5:011301, 2018.

[10] M. Higashiwaki and S. Fujita, editors. *Gallium Oxide*, volume 293. Springer International Publishing, 2020.

[11] W. Kong, G. Wu, K. Wang, T. Zhang, Y. Zou, D. Wang, and L. Luo. Graphene-β-Ga_2O_3 heterojunction for highly sensitive deep UV photodetector application. *Advanced Materials*, 28:10725–10731, 2016.

[12] Shinji Nakagomi, Taka aki Sato, Yusuke Takahashi, and Yoshihiro Kokubun. Deep ultraviolet photodiodes based on the β-Ga_2O_3/GaN heterojunction. *Sensors and Actuators A: Physical*, 232:208–213, 2015.

[13] A. Kalra, S. Vura, S. Rathkanthiwar, R. Muralidharan, S. Raghavan, and D. Nath. Demonstration of high-responsivity epitaxial β-Ga_2O_3/GaN metal-heterojunction-metal broadband UV-A/UV-C detector. *Applied Physics Express*, 11:064101, 2018.

[14] H. Maruska and J. Tietjen. The preparation and properties of vapor-deposited-single-crystalline GaN. *Applied Physics Letters*, 15:327–329, 1969.

[15] The Nobel Prize in Physics 2014. shorturl.at/kzIN7 Accessed: 07/05/2022.

[16] Y. Zhang, D. Piedra, M. Sun, J. Hennig, A. Dadgar, L. Yu, and T. Palacios. High-performance 500 V quasi- and fully-vertical GaN-on-si pn diodes. *IEEE Electron Device Letters*, 38:248–251, 2017.

[17] Y. Zhang, M. Sun, D. Piedra, M. Azize, T. Fujishima, and T. Palacios. GaN-on-Si vertical Schottky and p-n diodes. *IEEE Electron Device Letters*, 35:618–620, 2014.

[18] X. Zou, X. Zhang, X. Lu, C. Tang, and K. Lau. Fully vertical GaN p-i-n diodes using GaN-on-si epilayers. *IEEE Electron Device Letters*, 37:636–639, 2016.

[19] C. Liu, R. Khadar, and E. Matioli. GaN-on-Si quasi-vertical power MOSFETs. *IEEE Electron Device Letters*, 39:71–74, 2018.

[20] K. Shenai, R. Scott, and B. Baliga. Optimum semiconductors for high-power electronics. *IEEE Transactions on Electron Devices*, 36:1811–1823, 1989.
[21] X. She, A. Huang, O. Lucia, and B. Ozpineci. Review of silicon carbide power devices and their applications. *IEEE Transactions on Industrial Electronics*, 64:8193–8205, 2017.
[22] A. Huang. Power semiconductor devices for smart grid and renewable energy systems. *Proceedings of the IEEE*, 105:85–152, 2017.
[23] K. Kawahara, S. Hino, K. Sadamatsu, Y. Nakao, Y. Yamashiro, Y. Yamamoto, T. Iwamatsu, S. Nakata, S. Tomohisa, and S. Yamakawa. 6.5 kV Schottky-Barrier-Diode-Embedded SiC-MOSFET for compact full-unipolar module. In *29th International Symposium on Power Semiconductor Devices and ICs (ISPSD)*, 2017.
[24] W. Sung and B. Baliga. On developing one-chip integration of 1.2 kV SiC MOSFET and JBS diode (JBSFET). *IEEE Transactions on Industrial Electronics*, 64:8206–8212, 2017.
[25] N. Donato, N. Rouger, J. Pernot, G. Longobardi, and F. Udrea. Diamond power devices: state of the art, modelling, figures of merit and future perspective. *Journal of Physics D: Applied Physics*, 53:093001, 2019.
[26] T. Makino, S. Tanimoto, Y. Hayashi, H. Kato, N. Tokuda, M. Ogura, D. Takeuchi, K. Oyama, H. Ohashi, H. Okushi, and S. Yamasaki. Diamond Schottky-pn diode with high forward current density and fast switching operation. *Applied Physics Letters*, 94:262101, 2009.
[27] N. Ozawa, T. Makino, H. Kato, M. Ogura, Y. Kato, D. Takeuchi, H. Okushi, and S. Yamasaki. Temperature dependence of electrical characteristics for diamond Schottky-pn diode in forward bias. *Diamond and Related Materials*, 85:49–52, 2018.
[28] T. Matsumoto, T. Mukose, T. Makino, D. Takeuchi, S. Yamasaki, T. Inokuma, and N. Tokuda. Diamond Schottky-pn diode using lightly nitrogen-doped layer. *Diamond and Related Materials*, 75:152–154, 2017.
[29] J. Zhang, J. Shi, D. Qi, L. Chen, and K. Zhang. Recent progress on the electronic structure, defect, and doping properties of Ga_2O_3. *APL Materials*, 8:020906, 2020.
[30] Tamura Corporation. β-Ga_2O_3 Substrates. shorturl.at/bcyHU Accessed: 01/06/2021.
[31] J. Varley, J. Weber, A. Janotti, and C. Van de Walle. Oxygen vacancies and donor impurities in β-Ga_2O_3. *Applied Physics Letters*, 97:203111, 2010.
[32] C. Cocchi, H. Zschiesche, D. Nabok, A. Mogilatenko, M. Albrecht, Z. Galazka, H. Kirmse, C. Draxl, and C. Koch. Atomic signatures of local environment from core-level spectroscopy in β-Ga_2O_3. *Physical Review B*, 94:075147, 2016.
[33] B. Liu, M. Gu, and X. Liu. Lattice dynamical, dielectric, and thermodynamic properties of β-Ga_2O_3 from first principles. *Applied Physics Letters*, 91:172102, 2007.
[34] H. Morkoç. *Nitride Semiconductors and Devices*. Springer, 1999.
[35] T. Hanada. *Oxide and Nitride Semiconductors*. Springer, 2009.
[36] J. Rodrigues. *ZnO and GaN nanostructures for optoelectronic applications: synthesis and characterization*. PhD thesis, Universidade de Aveiro, 2015.
[37] F. Roccaforte and M. Leszczynski. *Nitride Semiconductor Technology*. John Wiley & Sons, Ltd, 2020.
[38] D. Fritsch, H. Schmidt, and M. Grundmann. Band-structure pseudopotential calculation of zinc-blende and wurtzite AlN, GaN, and InN. *Physical Review B*, 67:235205, 2003.
[39] Wei Guang-hong, Z. Jian, Zhang Kai-ming, and Xie Xi-de. Lattice dynamics of wurtzite semiconductors GaN and AlN. *Acta Physica Sinica (Overseas Edition)*, 7:841, 1998.
[40] L. Bergman, M. Dutta, and R. Nemanich. Raman Scattering Spectroscopy and Analyses

of III-V Nitride-Based Materials. In *Raman Scattering in Materials Science*. Springer Berlin Heidelberg, 2000.

[41] T. Ruf, J. Serrano, M. Cardona, P. Pavone, M. Pabst, M. Krisch, M. DAstuto, T. Suski, I. Grzegory, and M. Leszczynski. Phonon dispersion curves in wurtzite-structure GaN determined by inelastic X-ray scattering. *Physical Review Letters*, 86:906–909, 2001.

[42] H. Matsunami. Fundamental research on semiconductor SiC and its applications to power electronics. *Proceedings of the Japan Academy, Series B*, 96:235–254, 2020.

[43] G. Pensl, F. Ciobanu, T. Frank, M. Kriger, S. Reshanov, F. Schmid, and M. Weidner. *Sic Materials and Devices*. WORLD SCIENTIFIC, 2006.

[44] C. Zetterling and M. Östling. *Process Technology for Silicon Carbide Devices*. IET, 2002.

[45] G. Zhao and D. Bagayoko. Electronic structure and charge transfer in 3C- and 4H-SiC. *New Journal of Physics*, 2:16, 2000.

[46] J. Lüning, S. Eisebitt, J. Rubensson, C. Ellmers, and W. Eberhardt. Electronic structure of silicon carbide polytypes studied by soft x-ray spectroscopy. *Physical Review* , 59:10573, 1999.

[47] A. Sinelnik and A. Semenov. Theoretical study of the band structure of 2H-SiC and 4H-SiC of silicon carbide polytypes. *Condensed Matter Physics*, 24, 2021.

[48] R. Han, B. Han, D. Wang, and C. Li. Temperature dependence of Raman scattering from 4H-SiC with hexagonal defects. *Applied Physics Letters*, 99:011912, 2011.

[49] N. Protik, A. Katre, L. Lindsay, J. Carrete, N. Mingo, and D. Broido. Phonon thermal transport in 2H, 4H and 6H silicon carbide from first principles. 2017.

[50] J. Dong and A. Chen. Fundamental Properties of SiC: Crystal Structure, Bonding Energy, Band Structure, and Lattice Vibrations. In *SiC Power Materials*. Springer Berlin Heidelberg, 2004.

[51] Mi. Inagaki and F. Kang. Fundamental Science of Carbon Materials. In *Materials Science and Engineering of Carbon: Fundamentals*. Elsevier, 2014.

[52] N. Ashcroft and N. Mermin. *Solid State Physics*. Saunders College Publishing, 1976.

[53] H. Pierson. Structure and Properties of Diamond and Diamond Polytypes. In *Handbook of Carbon, Graphite, Diamonds and Fullerenes*. Elsevier, 1993.

[54] C. Breeding and J. Shigley. The "type" classification system of diamonds and its importance in gemology. *Gems &amp Gemology*, 45:96–111, 2009.

[55] J. Chelikowsky and S. Louie. First-principles linear combination of atomic orbitals method for the cohesive and structural properties of solids: application to diamond. *Physical Review B*, 29:3470, 1984.

[56] C. Clark, P. Dean, and P. Harris. Intrinsic edge absorption in diamond. *Proceedings of the Royal Society of London. Series A. Mathematical and Physical Sciences*, 277:312–329, 1964.

[57] Nikolai Teofilov. *Optical investigations on the wide bandgap semiconductors diamond and aluminum nitride*. PhD thesis, Universität Ulm, 2007.

[58] G. Painter, D. Ellis, and A. Lubinsky. Ab initio calculation of the electronic structure and optical properties of diamond using the discrete variational method. *Physical Review B*, 4:3610, 1971.

[59] D. Knight and W. White. Characterization of diamond films by Raman spectroscopy. *Journal of Materials Research*, 4:385–393, 1989.

[60] J. Warren, J. Yarnell, G. Dolling, and R. Cowley. Lattice dynamics of diamond. *Physical Review*, 158:805–808, 1967.

[61] T. Oishi, Y. Koga, K. Harada, and M. Kasu. High-mobility β-Ga_2O_3 single crystals grown by edge-defined film-fed growth method and their schottky barrier diodes with

ni contact. *Applied Physics Express*, 8:031101, 2015.
[62] C. Janowitz, V. Scherer, M. Mohamed, A.Krapf, H. Dwelk, R. Manzke, Z. Galazka, R. Uecker, K. Irmscher, R. Fornari, M. Michling, D. Schmeißer, J. Weber, J. Varley, and C. Van de Walle. Experimental electronic structure of In_2O_3 and Ga_2O_3. *New Journal of Physics*, 13:211903, 2011.
[63] K. Cheng. *III-V Compound Semiconductors and Devices*. Springer International Publishing, 2020.
[64] N. Son, W. Chen, O. Kordina, A. Konstantinov, B. Monemar, E. Janzén, D. Hofman, D. Volm, M. Drechsler, and B. Meyer. Electron effective masses in 4H-SiC. *Applied Physics Letters*, 66:1074–1076, 1995.
[65] N. Son, P. Hai, W. Chen, C. Hallin, B. Monemar, and E. Janzén. Hole effective masses in 4H-SiC determined by optically detected cyclotron resonance. *Materials Science Forum*, 338-342:563–566, 2000.
[66] F. Nava, C. Canali, C. Jacoboni, L. Reggiani, and S. Kozlov. Electron effective masses and lattice scattering in natural diamond. *Solid State Communications*, 33:475–477, 1980.
[67] L. Reggiani, D. Waechter, and S. Zukotynski. Hall-coefficient factor and inverse valence-band parameters of holes in natural diamond. *Physical Review B*, 28:3550, 1983.
[68] E. Smith and G. Dent. *Modern Raman Spectroscopy - A Practical Approach*. John Wiley & Sons, Ltd, 2005.
[69] D. K. Schroder. *Semiconductor Material and Device Characterization*. John Wiley & Sons, Inc., 2005.
[70] J. Ferraro. *Introductory Raman Spectroscopy*. Elsevier, 2003.
[71] J. Solé, L. Bausá, and D. Jaque. *An Introduction to the Optical Spectroscopy of Inorganic Solids*. J. Wiley, 2005.
[72] M. Fox. *Optical Properties of Solids*. Oxford University Press, 2010.
[73] I. Pelant and J. Valenta. Introduction. In *Luminescence Spectroscopy of Semiconductors*. Oxford University Press, 2012.
[74] P. Yu and M. Cardona. *Optical Properties II*. Springer Berlin Heidelberg, 2010.
[75] S. Perkowitz. Measurement Methods. In *Optical Characterization of Semiconductors*. Elsevier, 1993.
[76] C. Kranert, C. Sturm, R. Schmidt-Grund, and M. Grundmann. Raman tensor elements of β-Ga_2O_3. *Scientific Reports*, 6, 2016.
[77] Y. Yao, Y. Ishikawa, and Y. Sugawara. X-ray diffraction and Raman characterization of β-Ga_2O_3 single crystal grown by edge-defined film-fed growth method. *Journal of Applied Physics*, 126:205106, 2019.
[78] Z. Xu, Z. He, Y. Song, X. Fu, M. Rommel, X. Luo, A. Hartmaier, J. Zhang, and F. Fang. Topic review: Application of Raman spectroscopy characterization in micro/nano-machining. *Micromachines*, 9:361, 2018.
[79] A. Hassanien, A. Atta, M. El-Nahass, S. Ahmed, A. Shaltout, A. Al-Baradi, A. Alodhayb, and A. Kamal. Effect of annealing temperature on structural and optical properties of gallium oxide thin films deposited by RF-sputtering. *Optical and Quantum Electronics*, 52:1–16, 2020.
[80] V. Davydov, Y. Kitaev, I. Goncharuk, A. Smirnov, J. Graul, O. Semchinova, D. Uffmann, M. Smirnov, A. Mirgorodsky, and R. Evarestov. Phonon dispersion and Raman scattering in hexagonal GaN and AlN. *Physical Review B*, 58:12899, 1998.
[81] Y. Yin-Tang, H. Ru, and W. Ping. Raman analysis of defects in n-type 4H-SiC. *Chinese Physics B*, 17:3459, 2008.
[82] H. Harima. Properties of GaN and related compounds studied by means of Raman

scattering. *Journal of Physics: Condensed Matter*, 14:R967, 2002.

[83] J. Muth, J. Brown, M. Johnson, Z. Yu, R. Kolbas, J. Cook, and J. Schetzina. Absorption coefficient and refractive index of GaN, AlN and AlGaN alloys. *MRS Internet Journal of Nitride Semiconductor Research*, 4:502–507, 1999.

[84] L. Tung, K. Lin, E. Chang, W. Huang, Y. Hsiao, and C. Chiang. Photoluminescence and Raman studies of GaN films grown by MOCVD. *Journal of Physics: Conference Series*, 187:012021, 2009.

[85] C. Röder, F. Lipski, F. Habel, G. Leibiger, M. Abendroth, C. Himcinschi, and J. Kortus. Raman spectroscopic characterization of epitaxially grown GaN on sapphire. *Journal of Physics D: Applied Physics*, 46:285302, 2013.

[86] C. Kisielowski, J. Krüger, S. Ruvimov, T. Suski, J. Ager, E. Jones, Z. Liliental-Weber, M. Rubin, E. Weber, M. D. Bremser, and R. Davis. Strain-related phenomena in GaN thin films. *Physical Review B*, 54:17745, 1996.

[87] M. Chafai, A. Jaouhari, A. Torres, R. Antón, E. Martı
n, J. Jiménez, and W. C. Mitchel. Raman scattering from LO phonon-plasmon coupled modes and Hall-effect in n-type silicon carbide 4H-SiC. *Journal of Applied Physics*, 90:5211–5215, 2001.

[88] S. Sridhara, R. Devaty, and W. Choyke. Absorption coefficient of 4H silicon carbide from 3900 to 3250 Å. *Journal of Applied Physics*, 84:2963–2964, 1998.

[89] M. Irfan, M. Ajmal, M. Mazhar, M. Usmani, S. Ahmad, W. Abbas, M. Mahmood, and M. Hussain. Growth and characterization of 4H-SiC by thermal evaporation method. *Dig. J. Nanomater. Biostruct,*, 14:243–247, 2019.

[90] R. Sugie and T. Uchida. Determination of stress components in 4H-SiC power devices via Raman spectroscopy. *Journal of Applied Physics*, 122:195703, 2017.

[91] N. Sugiyama, M. Yamada, Y. Urakami, M. Kobayashi, T. Masuda, K. Nishikawa, F. Hirose, and S. Onda. Correlation of stress in silicon carbide crystal and frequency shift in micro-Raman spectroscopy. *MRS Proceedings*, 1693, 2014.

[92] A. Dychalska, P. Popielarski, W. Franków, K. Fabisiak, K. Paprocki, and M. Szybowicz. Study of CVD diamond layers with amorphous carbon admixture by Raman scattering spectroscopy. *Materials Science-Poland*, 33:799–805, 2015.

[93] N. Ueda, H. Hosono, R. Waseda, and H. Kawazoe. Anisotropy of electrical and optical properties in β-Ga_2O_3 single crystals. *Applied Physics Letters*, 71:933–935, 1997.

[94] W. Klahold, W. Choyke, and R. Devaty. Band structure properties, phonons, and exciton fine structure in 4H-SiC measured by wavelength-modulated absorption and low-temperature photoluminescence. *Physical Review B*, 102:205203, 2020.

[95] P. Grivickas, K. Redeckas, K. Gulbinas, A. Conway, L. Voss, M. Bora, S. Sampayan, M. Vengris, and V. Grivickas. Intrinsic shape of free carrier absorption spectra in 4H-SiC. *Journal of Applied Physics*, 125:225701, 2019.

[96] T. Kimoto, A. Itoh, H. Matsunami, S. Sridhara, L. Clemen, R. Devaty, W. Choyke, T. Dalibor, C. Peppermüller, and G. Pensl. Nitrogen donors and deep levels in high-quality 4H-SiC epilayers grown by chemical vapor deposition. *Applied Physics Letters*, 67:2833–2835, 1995.

[97] E. Biedermann. The optical absorption bands and their anisotropy in the various modifications of SiC. *Solid State Communications*, 3:343–346, 1965.

[98] Y. Wang, P. Dickens, J. Varley, X. Ni, E.l Lotubai, S. Sprawls, F. Liu, V. Lordi, S. Krishnamoorthy, S. Blair, K. Lynn, M. Scarpulla, and B. Sensale-Rodriguez. Incident wavelength and polarization dependence of spectral shifts in β-Ga_2O_3 UV photoluminescence. *Scientific Reports*, 8:1–7, 2018.

[99] R. Williams and K. Song. The self-trapped exciton. *Journal of Physics and Chemistry*

of Solids, 51:679–716, 1990.

[100] J. Zanoni, D. Esteves, B. Falcão, J. Leitão, L. Rino, Z. Jia, W. Um, L. Alves, K. Lorenz, M. Correia, M. Peres, T. Monteiro, and J. Rodrigues. Detailed RT spectroscopic analysis of doped β-Ga_2O_3 with Mg, Sn and Fe. 2022.

[101] M. McCluskey. Point defects in Ga_2O_3. *Journal of Applied Physics*, 127:101101, 2020.

[102] K. Goto, K. Konishi, H. Murakami, Y. Kumagai, B. Monemar, M. Higashiwaki, A. Kuramata, and S. Yamakoshi. Halide vapor phase epitaxy of Si doped β-Ga_2O_3 and its electrical properties. *Thin Solid Films*, 666:182–184, 2018.

[103] J. Ritter, J. Huso, P. Dickens, J. Varley, K. Lynn, and M. McCluskey. Compensation and hydrogen passivation of magnesium acceptors in β-Ga_2O_3. *Applied Physics Letters*, 113:052101, 2018.

[104] L. Binet and D. Gourier. Origin of the blue luminescence of β-Ga_2O_3. *Journal of Physics and Chemistry of Solids*, 59:1241–1249, 1998.

[105] N. Son, K. Goto, H. Murakami, Y. Kumagai, and B. Monemar. *Defects and impurities in* $\beta - Ga_2O_3$, chapter 3 - Progress in semiconductor β-Ga_2O_3. Elsevier, 2019.

[106] Y. Tokida and S. Adachi. Photoluminescence properties and energy-level analysis of Ga_2O_3:Tb^{3+} green phosphor prepared by metal organic deposition. *ECS Journal of Solid State Science and Technology*, 3:R100, 2014.

[107] Y. Tokida and S. Adachi. Photoluminescence spectroscopy and energy-level analysis of metal-organic-deposited Ga_2O_3:Cr^{3+} films. *Journal of Applied Physics*, 112:063522, 2012.

[108] E. Nogales, J. García, B. Méndez, and J. Piqueras. Red luminescence of Cr in β-Ga_2O_3 nanowires. *Journal of Applied Physics*, 101:033517, 2007.

[109] S. Sugano and Y. Tanabe. Absorption spectra of Cr^{3+} part a. theoretical studies of the absorption bands and lines. *Journal of the Physical Society of Japan*, 13:880–899, 1958.

[110] H. Tippins. Optical and microwave properties of trivalent chromium in β-Ga_2O_3. *Physical Review*, 137:A865, 1965.

[111] V. Vasyltsiv, Y. Rym, and Y. Zakharko. Absorption and luminescence of Cr^{3+}-doped solid solutions of gallium-indium oxides. In Richard Scheps, editor, *Solid State Lasers V*. SPIE, 1996.

[112] M. Reshchikov and H. Morkoç. Luminescence properties of defects in GaN. *Journal of Applied Physics*, 97:2293–2295, 2005.

[113] J. Pankove and J. Hutchby. Photoluminescence of ion-implanted GaN. *Journal of Applied Physics*, 47:5387–5390, 1976.

[114] T. Ogino and M. Aoki. Mechanism of yellow luminescence in GaN. *Japanese Journal of Applied Physics*, 19:2395, 1980.

[115] J. Lyons, A. Janotti, and C. Van de Walle. Carbon impurities and the yellow luminescence in GaN. *Applied Physics Letters*, 97:152108, 2010.

[116] Friederike Zimmermann, Jan Beyer, Christian Röder, Franziska C. Beyer, Eberhard Richter, Klaus Irmscher, and Johannes Heitmann. Current status of carbon-related defect luminescence in GaN. *physica status solidi (a)*, 218:2100235, 2021.

[117] B. Monemar, P. Paskov, J. Bergman, A. Toropov, T. Shubina, T. Malinauskas, and A. Usui. Recombination of free and bound excitons in GaN. *physica status solidi (b)*, 245:1723–1740, 2008.

[118] M. Suzuki, T. Uenoyama, and A. Yanase. First-principles calculations of effective-mass parameters of AlN and GaN. *Physical Review B*, 52:8132, 1995.

[119] B. Meyer, J. Sann, D. Hofmann, C. Neumann, and A. Zeuner. Shallow donors and acceptors in ZnO. *Semiconductor Science and Technology*, 20:S62, 2005.

[120] S. Kasap and P. Capper. *Springer Handbook of Electronic and Photonic Materials*. Springer, 2006.

[121] S. Zhuo, X. Liu, W. Huang, H. Kong, J. Xin, and E. Shi. Photoluminescence in fluorescent 4H-SiC single crystal adjusted by B, Al, and N ternary dopants. *Chinese Physics B*, 28:017101, 2019.

[122] S. Hagen, A. Van Kemenade, and J. Van Der Does De Bye. Donor-acceptor pair spectra in 6H and 4H SiC doped with nitrogen and aluminium. *Journal of Luminescence*, 8:18–31, 1973.

[123] M. Ikeda, H. Matsunami, and T. Tanaka. Site effect on the impurity levels in 4H, 6H and 15R SiC. *Physical Review B*, 22:2842, 1980.

[124] A. Kakanakova-Georgieva, R. Yakimova, A. Henry, M. Linnarsson, M. Syväjärvi, and E. Janzén. Cathodoluminescence identification of donor-acceptor related emissions in as-grown 4H-SiC layers. *Journal of Applied Physics*, 91:2890–2895, 2002.

[125] Ch. Haberstroh, R. Helbig, and R. Stein. Some new features of the photoluminescence of SiC(6H), SiC(4H), and SiC(15R). *Journal of Applied Physics*, 76:509–513, 1994.

[126] S. Sridhara, L. Clemen, R. Devaty, W. Choyke, D. Larkin, H. Kong, T. Troffer, and G. Pensl. Photoluminescence and transport studies of boron in 4H-SiC. *Journal of Applied Physics*, 83:7909–7919, 1998.

[127] A. Yang, K. Murata, T. Miyazawa, T. Tawara, and H. Tsuchida. Analysis of carrier lifetimes in Nb-doped n-type 4H-SiC epilayers. *Journal of Applied Physics*, 126:055103, 2019.

[128] A. Suzuki, H. Matsunami, and T. Tanaka. Photoluminescence due to Al, Ga, and B acceptors in 4H-, 6H-, and 3C-SiC grown from a Si melt. *Journal of The Electrochemical Society*, 124:241, 1977.

[129] A. Yang, K. Murata, T. Miyazawa, T. Tawara, and H. Tsuchida. Time-resolved photoluminescence spectral analysis of phonon-assisted DAP and e-A recombination in nb-doped *n*-type 4H-SiC epilayers. *Journal of Physics D: Applied Physics*, 52:10LT01, 2019.

[130] A. Itoh, H. Akita, T. Kimoto, and H. Matsunami. High-quality 4H-SiC homoepitaxial layers grown by step-controlled epitaxy. *Applied Physics Letters*, 65:1400–1402, 1994.

[131] S. Asada, T. Kimoto, and I. Ivanov. Calibration on wide-ranging aluminum doping concentrations by photoluminescence in high-quality uncompensated p-type 4H-SiC. *Applied Physics Letters*, 111:072101, 2017.

[132] Edmund Optics. Understanding Neutral Density Filters. shorturl.at/jqGRW Acessed 06/06/2022.

[133] T. Schmidt, K. Lischka, and W. Zulehner. Excitation-power dependence of the near-band-edge photoluminescence of semiconductors. *Physical Review B*, 45:8989, 1992.

[134] G. Davies. The jahn-teller effect and vibronic coupling at deep levels in diamond. *Reports on Progress in Physics*, 44:787, 1981.

[135] J. Walker. Optical absorption and luminescence in diamond. *Reports on Progress in Physics*, 42:1605, 1979.

[136] J. Loubser and J. Wyk. Electron spin resonance in the study of diamond. *Reports on Progress in Physics*, 41:1201, 1978.

[137] C. Lin, H. Chang, M. Hayashi, and S. Lin. Excitation properties of the H3 defect center in diamond: A theoretical study. *Chemical Physics Letters*, 475:68–72, 2009.

[138] M. Doherty, N. Manson, P. Delaney, F. Jelezko, J. Wrachtrup, and L. Hollenberg. The nitrogen-vacancy colour centre in diamond. *Physics Reports*, 528:1–45, 2013.

[139] A. Pant, C. Gupta, K. Senkalla, G. Felsted, X. Xia, T. Spohn, S. Dunham, F. Jelezko, and P. Pauzauskie. Reduced photothermal heating in diamonds enriched with H3 point

defects. *Journal of Applied Physics*, 131:234401, 2022.